

Telomere Dysfunction Drives Aberrant Hematopoietic Differentiation and Myelodysplastic Syndrome

Highlights

- Mice with dysfunctional telomeres exhibit hallmark features of human MDS
- DNA damage directly induces skewed myeloid progenitor differentiation
- Telomere dysfunction represses RNA splicing gene expression in CMP
- Aberrant RNA splicing due to reduced *srsf2* expression induces telomere dysfunction

Authors

Simona Colla,
Derrick Sek Tong Ong, ...,
Guillermo Garcia-Manero,
Ronald A. DePinho

Correspondence

scolla@mdanderson.org (S.C.),
rdepinho@mdanderson.org (R.A.D.)

In Brief

Colla et al. provide genetic evidence that persistent physiological DNA damage drives classical myelodysplastic syndrome features and biases common myeloid progenitor differentiation toward the myeloid lineage, attributed to repression of expression of mRNA splicing/processing genes and aberrant RNA splicing.

Accession Numbers

GSE62393
ftp://ftp.ncbi.nih.gov/pub/TraceDB/misc/tmp/SRP048846_SRP048858



Telomere Dysfunction Drives Aberrant Hematopoietic Differentiation and Myelodysplastic Syndrome

Simona Colla,^{1,13,*} Derrick Sek Tong Ong,^{2,13} Yamini Ogoti,¹ Matteo Marchesini,¹ Nipun A. Mistry,³ Karen Clise-Dwyer,⁴ Sonny A. Ang,⁵ Paola Storti,^{2,6} Andrea Viale,² Nicola Giuliani,⁶ Kathryn Ruisaard,⁴ Irene Ganan Gomez,¹ Christopher A. Bristow,⁷ Marcos Estecio,^{1,8} David C. Weksberg,² Yan Wing Ho,² Baoli Hu,² Giannicola Genovese,² Piergiorgio Pettazzoni,² Asha S. Multani,⁹ Shan Jiang,² Sujun Hua,² Michael C. Ryan,¹⁰ Alessandro Carugo,² Luigi Nezi,² Yue Wei,¹ Hui Yang,¹ Marianna D'Anca,¹ Li Zhang,³ Sarah Gaddis,⁸ Ting Gong,⁸ James W. Horner,⁷ Timothy P. Heffernan,⁷ Philip Jones,⁷ Laurence J.N. Cooper,⁵ Han Liang,³ Hagop Kantarjian,¹ Y. Alan Wang,² Lynda Chin,² Carlos Bueso-Ramos,¹¹ Guillermo Garcia-Manero,¹ and Ronald A. DePinho^{12,*}

¹Department of Leukemia, University of Texas MD Anderson Cancer Center, Houston, TX 77030, USA

²Department of Genomic Medicine, University of Texas MD Anderson Cancer Center, Houston, TX 77030, USA

³Department of Bioinformatics and Computational Biology, University of Texas MD Anderson Cancer Center, Houston, TX 77030, USA

⁴Department of Stem Cell Transplantation and Cellular Therapy, University of Texas MD Anderson Cancer Center, Houston, TX 77030, USA

⁵Department of Pediatric Research, University of Texas MD Anderson Cancer Center, Houston, TX 77030, USA

⁶Hematology, Department of Clinical and Experimental Medicine, University of Parma, 43126 Parma, Italy

⁷Institute for Applied Cancer Science, University of Texas MD Anderson Cancer Center, Houston, TX 77030, USA

⁸Department of Molecular Carcinogenesis, University of Texas MD Anderson Cancer Center, Smithville, TX 78957, USA

⁹Department of Genetics, University of Texas MD Anderson Cancer Center, Houston, TX 77030, USA

¹⁰In Silico Solutions, Falls Church, VA 22043, USA

¹¹Department of Hematopathology, University of Texas MD Cancer Center, Houston, TX 77030, USA

¹²Department of Cancer Biology, University of Texas MD Anderson Cancer Center, Houston, TX 77030, USA

¹³Co-first author

*Correspondence: scolla@mdanderson.org (S.C.), rdepinho@mdanderson.org (R.A.D.)

<http://dx.doi.org/10.1016/j.ccell.2015.04.007>

SUMMARY

Myelodysplastic syndrome (MDS) risk correlates with advancing age, therapy-induced DNA damage, and/or shorter telomeres, but whether telomere erosion directly induces MDS is unknown. Here, we provide the genetic evidence that telomere dysfunction-induced DNA damage drives classical MDS phenotypes and alters common myeloid progenitor (CMP) differentiation by repressing the expression of mRNA splicing/processing genes, including *SRSF2*. RNA-seq analyses of telomere dysfunctional CMP identified aberrantly spliced transcripts linked to pathways relevant to MDS pathogenesis such as genome stability, DNA repair, chromatin remodeling, and histone modification, which are also enriched in mouse CMP haploinsufficient for *SRSF2* and in CD34⁺ CMML patient cells harboring *SRSF2* mutation. Together, our studies establish an intimate link across telomere biology, aberrant RNA splicing, and myeloid progenitor differentiation.

INTRODUCTION

Advancing age is associated with the accumulation of DNA damage and attendant cellular checkpoint responses of apoptosis

and senescence, as well as declining mitochondrial function and oxidative defense (Jaskelioff et al., 2011). Model systems have established that these DNA damage corollaries contribute to tissue degenerative phenotypes (Sahin and DePinho, 2012).

Significance

Myelodysplastic syndrome (MDS) is a heterogeneous group of hematopoietic neoplastic disorders. While MDS risk correlates with advancing age, therapy-induced DNA damage, and/or shorter telomeres, whether DNA damage signaling can directly provoke MDS is unknown. Employing an inducible telomerase reverse transcriptase-estrogen receptor (TERT^{ER}) model, we demonstrate that persistent physiological DNA damage (from eroded telomeres) drives classical MDS features and biases common myeloid progenitor (CMP) differentiation toward the myeloid lineage. This defective CMP differentiation was attributed to repression of expression of mRNA splicing/processing genes, resulting in aberrant RNA splicing. Our studies establish an intimate link across telomere biology, aberrant RNA splicing, and cellular differentiation, and suggest that strategies that mitigate DNA damage signaling may be useful for prevention/treatment of MDS.

A source of age-associated DNA damage signaling can derive from progressive telomere erosion and damage which appears to provide a reservoir of persistent DNA damage signaling in the context of aging cells (Chin et al., 1999; d'Adda di Fagagna et al., 2003; Karlseder et al., 2002; Rudolph et al., 1999). These processes are particularly evident in tissues with high cell turnover rate, including the hematopoietic system (Lee et al., 1998; Rudolph et al., 1999). Indeed, accumulating evidence supports the view that DNA damage checkpoints activated by telomere erosion can drive hematopoietic stem cell (HSC) decline, thereby compromising HSC self-renewal, repopulating capacity, and differentiation (Rossi et al., 2007; Wang et al., 2012). While acute DNA damage can trigger a p53-mediated apoptosis or senescence of hematopoietic progenitor cells (Insinga et al., 2013; Milyavsky et al., 2010), whether and how accumulating physiological or pathological DNA damage (including telomeres) might influence the differentiation decisions of hematopoietic progenitor cells has not been explored. Of relevance to this study, it is worth noting that the specific type of cellular response (e.g., apoptosis, cell cycle, etc.) in telomere dysfunctional mice can vary depending on cell type (Lee et al., 1998).

Myelodysplastic syndrome (MDS) is a very heterogeneous group of hematopoietic disorders characterized by ineffective myeloid differentiation, dysplasia, and excessive DNA damage accumulation in stem/progenitor cells (Zhou et al., 2013). MDS incidence has risen dramatically in recent years (Rollison et al., 2008) and is associated with advanced age, shorter telomeres, cancer chemotherapy with alkylating agents, radiation, and inherited syndromes related to abnormalities in DNA repair (Zhou et al., 2013). On the genomic level, MDS alterations include chromosomal abnormalities (loss of 5q, 7 or 7q, 20q, and/or Y, and trisomy 8), point mutations of *NRAS* or *KRAS* and/or *TP53* as well as genes involved in DNA methylation (*DNMT3A*, *TET2*, *IDH1*, and *IDH2*), chromatin remodeling (*ASXL1* and *EZH2*), splicing regulation (*SF3B1*, *SRSF2*, *U2AF1*, *U2AF2*, *SF3A1*, *ZRSR2*, *SF1*, and *PRPF40B*) (Bejar et al., 2011; Larsson et al., 2013), and telomerase complex (*TERT*, *RTKL1*, and *TINF2*). While the HSCs harboring these mutations are the cell-of-origin for MDS (Will et al., 2012) and are responsible for clonal dominance, derivative committed progenitors from these HSCs manifest skewed differentiation resulting in the morphological and clinical phenotype of MDS. Herein, we sought to understand if telomere dysfunction and persistent DNA damage signaling activation can be the primary instigators of MDS in the absence of MDS-associated gene mutations or genetic alterations, and how hematopoietic progenitor cells can contribute to ineffective differentiation that maintains MDS and eventually results in disease progression.

RESULTS

Telomere Dysfunctional Mice Exhibit Hallmarks of Human MDS

Recognizing that the biological response to telomere dysfunction is highly cell type dependent (Lee et al., 1998), we sought to catalog the cell biological and molecular responses to telomere dysfunction in various hematopoietic lineages and assess their potential role in MDS pathogenesis. To model chronic phys-

iological DNA damage in the hematopoietic system, we employed the inducible telomerase model, *TERT^{ER}*, engineered to encode a telomerase reverse transcriptase-estrogen receptor fusion protein that can be activated by 4-hydroxytamoxifen (OHT) treatment. Inter-generational crosses of *TERT^{ER/ER}* mice leads to progressive telomere erosion, which by the fourth and fifth generations (G4/G5) elicits telomere dysfunction and associated DNA damage signaling and severe tissue degeneration (Jaskelioff et al., 2011). In the late generation G4/G5 *TERT^{ER/ER}* mice, systemic administration of OHT restores telomeres, quells DNA damage signaling, and reverses tissue degeneration phenotypes (Jaskelioff et al., 2011).

We first audited in-depth the phenotypic impact of telomere dysfunction on the hematopoietic system in 3-month- and 7-month-old G4/G5 *TERT^{ER/ER}* mice. These analyses revealed significant cytopenias in the peripheral blood, a decline in lymphopoiesis, slight anemia, and moderate granulomonocytosis in advancing age (Figure 1A). Bone marrow (BM) hypercellularity and increased myeloid-to-erythroid progenitor (M:E) ratio (Figure 1B), in the absence of increased apoptosis (Figure S1A), were consistent with a condition of myeloid-skewed differentiation and ineffective hematopoiesis. Further BM analysis revealed severe tri-lineage dysplasia (Figure 1C: hypersegmented neutrophils [29% ± 7.39%], erythroblasts [18.25% ± 7.13], and megakaryocytes [44.75% ± 20.27%]), absence of ring sideroblasts (Figure S1B), and increase of immature, morphologically abnormal myeloid blasts (Figure 1D, top: % of blasts: 10%–15% and myeloperoxidase positive blasts: 78% ± 10.81%) frequently with pronounced monocytic differentiation (Figure 1D, bottom: butyrate esterase positive blasts: 35.75% ± 3.30%), which recapitulated the hallmark features of refractory anemia with excess of blasts (RAEB) in 80% of cases or chronic myelomonocytic leukemia (CMML) in 20% of cases, specific sub-groups of MDS that are characterized by a high propensity to develop acute myeloid leukemia (AML). Accordingly, approximately 5% of aged G4/G5 *TERT^{ER/ER}* mice progressed to AML, as demonstrated by a marked increase of BM myeloid blasts (more than 20% of BM cellularity) (Figure 1E) and infiltration of myeloid precursors into the splenic white-red pulp architecture, resulting in myeloid sarcoma with the complete effacement of lymphoid follicles (Figure 1F). Cytogenetic analysis of G4/G5 *TERT^{ER/ER}* BM cells showed chromosomal breaks and fusions (Figure S1C), which eventually fuel chromosomal translocations (Figure S1D).

Telomerase Reactivation Rescues Impaired Progenitor Cell Differentiation in Telomere Dysfunctional Mice

To study the cellular mechanisms underlying skewed myeloid differentiation induced by telomere attrition and given the important contribution of the hematopoietic progenitor compartment toward ineffective hematopoiesis and MDS phenotype, we examined the c-Kit⁺Sca[−]Lin[−] (KS[−]L) compartment that represents a key branch at which HSC-derived progenitors commit to various myeloid lineages (Akashi et al., 2000) (Figure S2A). Compared to age- and gender-matched G0 *TERT^{ER/+}* controls, the KS[−]L compartment of G4/G5 *TERT^{ER/ER}* mice showed a significant increase in the frequency (Figure 2A) and absolute number (Figure S2B) of granulocyte-macrophage progenitors

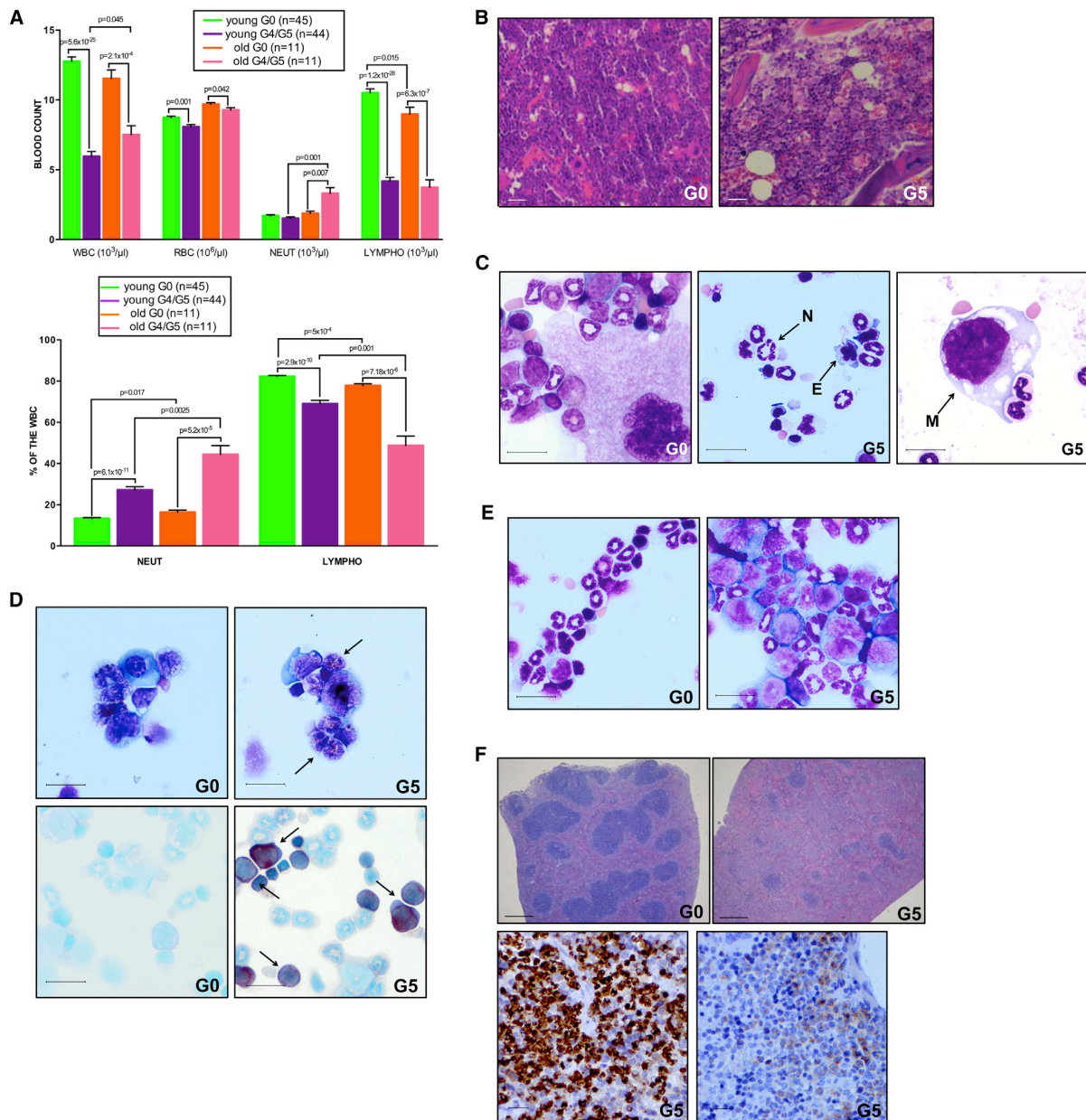


Figure 1. The Hematopoietic Compartment of Telomere Dysfunctional Mice Recapitulates Hallmark Features of Human MDS

(A) Complete blood count evaluation of age-matched young (3-month-old) and old (7-month-old) mice of indicated genotypes (top panel) (error bars denote SEM). Relative abundance of neutrophils and lymphocytes in total white blood cells of young and old mice of indicated genotypes (bottom panel) (error bars denote SEM). (B) Hematoxylin and eosin (H&E) stained sections of BM biopsies of representative G0 (left panel) and G5 (right panel) mice. The scale bar represents 50 micrometers (μm). (C) Pattern of multi-lineage differentiation in a representative G0 BM cytospin (left panel); dysplastic neutrophil (N), erythroblast (E), and megakaryocyte (M) in a representative G5 BM cytospin (central and right panels). The scale bar represents 15 μm . (D) Myeloperoxidase (MPO) (top panel) and butyrate esterase (bottom panel) cytochemical staining of a representative G0 (on the left) or G5 (on the right) BM cytospin. Arrows indicate positive blasts. The scale bar represents 15 μm . (E) Pattern of multi-lineage differentiation in a representative G0 BM cytospin (left panel); increased number of BM blasts (>20% of BM cellularity) in the BM cytospin of a representative G5 mouse in transformation (right panel). The scale bar represents 15 μm . (F) H&E stained splenic section of a representative G0 mouse (top, left panel) or G5 mouse in transformation (top, right panel). The scale bar represents 200 μm . Myeloid cells infiltrating the white-red pulp are positive for CD11b (bottom, left panel) and MPO (bottom, right panel). The scale bar represents 15 μm . See also Figure S1.

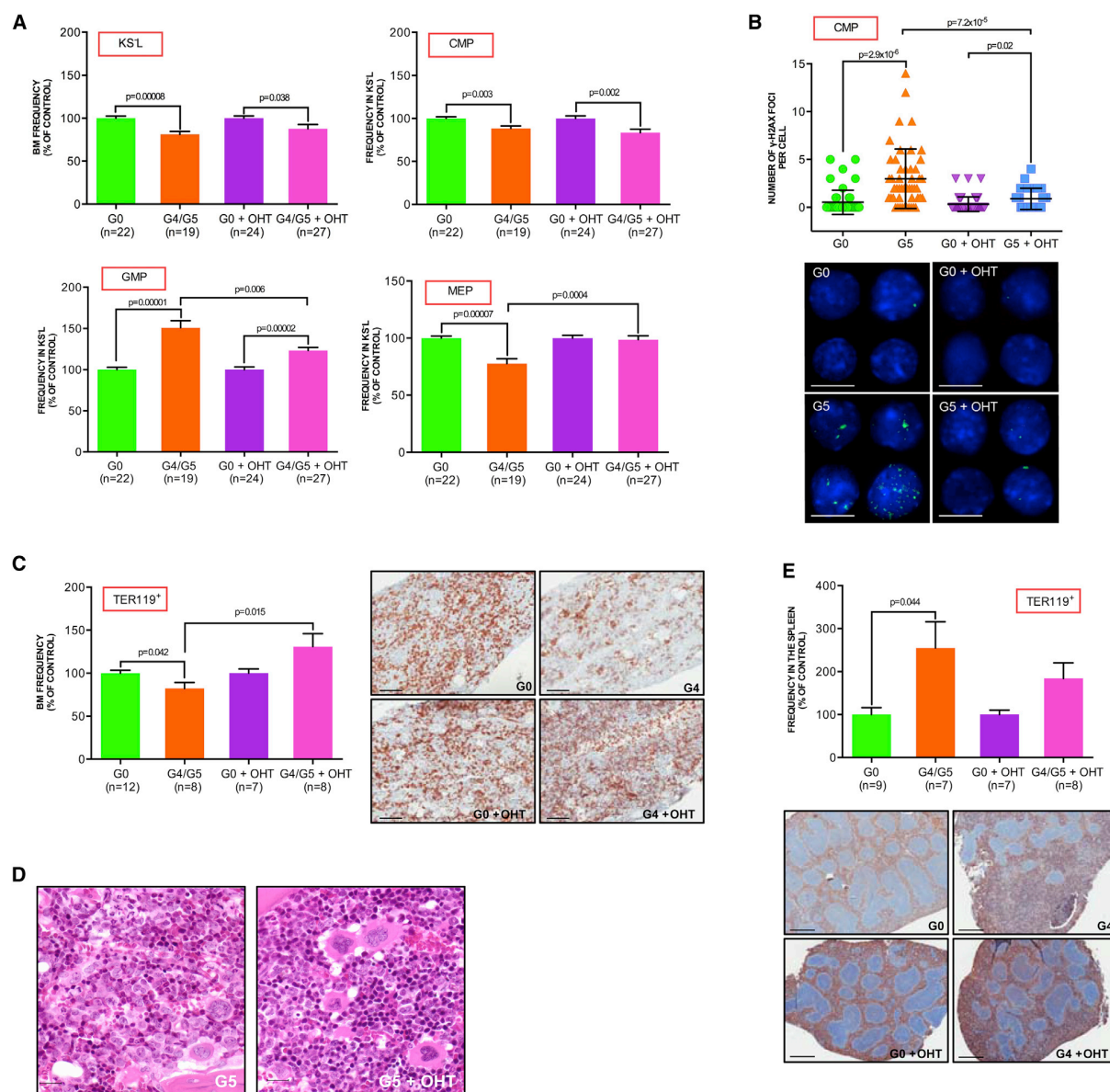


Figure 2. Skewed Myeloid-Erythroid Differentiation of CMP Is Reversed by Telomerase Reactivation

(A) KS⁻L frequency in the BM, as well as the CMP, GMP, and MEP frequencies in the KS⁻L population of indicated genotypes and treatments (mean and SEM of age-matched 3-month-old mice from six independent experiments of telomerase reactivation in vivo; data are expressed as percentage of corresponding controls).

(B) Anti-γH2AX immunofluorescence in CMP sorted from mice of indicated genotypes and treatments: numbers of γH2AX foci per cell (upper panel; error bars denote SD) and representative images (bottom panel): α-γH2AX: green and DAPI: blue. The scale bar represents 20 μm.

(C and E) Frequency of the erythroid lineage in the BM (C, left) and spleen (E, upper) of indicated genotypes and treatments (mean and SEM of mice from two independent experiments of telomerase reactivation in vivo; data are expressed as percentage of corresponding controls), representative Ter119-stained sections of BM (C, right; scale bar represents 100 μm) and spleen (E, bottom) from age-matched controls and experimental mice (the scale represents 200 μm).

(D) H&E stained BM section of a representative G5 mouse without (left panel) or with OHT treatment (right panel; the scale bar represents 15 μm). See also Figure S2.

(GMP; KS⁻L CD34⁺FcγR^{hi}), with the concomitant loss of megakaryocyte-erythroid progenitors (MEP; KS⁻L CD34⁺FcγR^{-/lo}) and slight reduction of common myeloid progenitors (CMP;

KS⁻L CD34⁺FcγR^{-/lo}), in the absence of increased apoptosis in these populations (data not shown). These observations gain added significance in light of recent findings that a significant

expansion of the GMP compartment occurs in the RAEB stage of MDS patients with higher risk of leukemic transformation (Pang et al., 2013; Will et al., 2012). Notably, the GMP population further increased in the aged G4/G5 TERT^{ER/ER} mice (Figure S2C) or during leukemic transformation (data not shown). Further analysis of the hematopoietic sub-populations showed a preferential accumulation of γ -H2AX and 53BP1 DNA damage foci in the telomere dysfunctional CMP (Figures 2B and S2D), but not in GMP or MEP (Figures S2E and S2F), suggesting that various sub-types of hematopoietic progenitors may respond differently to telomere erosion.

To determine whether elevated telomere associated DNA damage was the instigator for skewed myeloid-erythroid differentiation, we reactivated telomerase in 3-month-old telomere dysfunctional mice to restore telomere function and thus quell DNA damage signaling. Following 40 days of continuous OHT exposure, total BM cells showed increased telomere length as measured by flow-fluorescence in situ hybridization (FISH) and a significant reduction of signal-free ends (Figures S2G and S2H). Telomere restoration was associated with a significant increase in MEP frequency (Figure 2A), MEP absolute number (Figure S2B), and a corresponding reduction of GMP. Furthermore, characterization of the progenitor compartment in the early generation telomerase deficient mice (G1) without telomere dysfunction showed no aberrant myeloid differentiation (Figure S2I), suggesting that skewed myeloid differentiation in G4/G5 mice is attributed to DNA damage activation, and not the absence of telomerase per se. Together, these data support the view that telomere attrition-induced DNA damage itself can serve as a driver of altered myeloid progenitor differentiation, resulting in a persistent accumulation of the myeloid lineage at the expense of the MEP population, a process fundamental to MDS pathogenesis.

Telomerase reactivation was also associated with significantly reduced γ -H2AX and 53BP1 foci of the CMP population (Figures 2B and S2D). The recovery of the MEP population upon sustained OHT treatment tracked with a significant restoration of BM Ter119⁺ erythroid progenitors (Figure 2C) in all developmental stages (data not shown), an improvement of M:E ratio and reduction of immature myeloid cells in the BM (Figure 2D) and decline of splenic extra-medullary erythropoiesis (Figure 2E). Thus, endogenous telomerase reactivation and extinction of DNA damage signaling restores the normal myeloid differentiation process, reinforcing the link between telomere dysfunction and aberrant myeloid differentiation. Nevertheless, the failure of telomerase reactivation to rescue the KSL decline (Figure 2A) implicates the existence of additional upstream differentiation checkpoints involving the stem cell compartment as previously reported (Rossi et al., 2007; Wang et al., 2012). Consistent with the expansion of phenotypically primitive HSCs occurring in MDS (Will et al., 2012), the telomere dysfunctional HSC compartment (KSL) showed an increased expansion in the steady-state frequency of long-term HSC (LT-HSC; c-Kit⁺Sca⁺Lin⁻CD34⁺flk2⁻) and short-term HSC (ST-HSC; c-Kit⁺Sca⁺Lin⁻CD34⁺flk2⁻), with the concomitant decrease of multi-potent progenitor cells (MPP; c-Kit⁺Sca⁺Lin⁻CD34⁺flk2⁺) (Figures S2J and S2K), and compromised repopulation capability upon BM competitive transplantation (Figure S2L).

Defective CMP Differentiation Is due to Cell Intrinsic DNA Damage Signaling Activation

Impaired progenitor differentiation could occur as a result of a telomere dysfunctional systemic environment that limits HSC function and organ homeostasis (Ju et al., 2007) and/or cell intrinsic defects of telomere dysfunctional hematopoietic cells (Allsopp et al., 2003). To distinguish between the two possibilities, we transplanted LT-HSC isolated from 3-month-old G0 or G4/G5 mice into wild-type congenic recipients and assayed recipient BM for donor-derived progenitor cell frequencies 2 months post-transplantation. Analysis of the G4/G5 derived hematopoietic system revealed that the level of donor-derived skewed myeloid differentiation was comparable to that observed at steady state in the same young telomere dysfunctional mice before transplantation (Figure 3A). Furthermore, G4/G5 transplanted BM showed severe tri-lineage dysplasia and an increase of immature, morphologically abnormal myeloid blasts. Notably, one of the six mice transplanted with G5 HSC progressed to AML, as demonstrated by a marked increase of BM myeloid blasts and infiltration of myeloid precursors into the splenic white-red pulp architecture (Figure 3B). Overall, these findings demonstrate that telomere dysfunction exerts a prominent cell-intrinsic effect on the differentiation commitment of progenitor cells and are consistent with the existence of “diseased” stem cells that are capable of regenerating the MDS phenotype after transplantation in wild-type mice.

Additionally, in the light of recent findings showing that megakaryocyte and MEP can also directly differentiate from HSC (Yamamoto et al., 2013), we evaluated if the CMP is responsible for the skewed myeloid differentiation of telomere dysfunctional mice as suggested from the in vivo experiments. To this end, we sorted G0 and G4/G5 CMP and determined their differentiation potential in methylcellulose clonogenic assay. Consistent with the in vivo results (Figure 2A), there was a profound impairment of myeloid differentiation toward the erythroid lineage in favor of granulo-monocytic commitment in the telomere dysfunctional CMP which was partially rescued upon telomerase reactivation (Figure 3C; data not shown). Similar results were obtained in clonogenic assays of BM mononuclear cells (MNCs) (Figure S3A), as well as HSCs upon long-term culture (LTC-IC) (data not shown). On the basis of these in vivo and in vitro data, we conclude that telomere dysfunction affects myeloid differentiation. Next, we explored the nature of DNA damage signaling and its impact on CMP differentiation processes. We observed that a highly specific inhibitor of the ataxia telangiectasia and Rad3 related (ATR), but not ataxia telangiectasia mutated (ATM) kinase, partially improved erythroid differentiation of telomere dysfunctional CMP (Figure 3D), a finding consistent with a known role for ATR in telomere dysfunction and aging-induced replicative stress signaling (Kastan and Bartek, 2004) ($p = 2.2 \times 10^{-10}$; Figure S3B). Correspondingly, our clinical correlative studies showed that ATR phosphorylation (p-ATR) status in the CD34⁺ cells correlates with high risk MDS, which is characterized by an expanded GMP population at the expense of MEP (Pang et al., 2013; Will et al., 2012). We observed p-ATR signal in only five of 25 patients samples exhibiting low risk MDS versus 23 of 32 with high risk MDS ($p = 0.00014$) (Figure S3C). Collectively, these data indicate

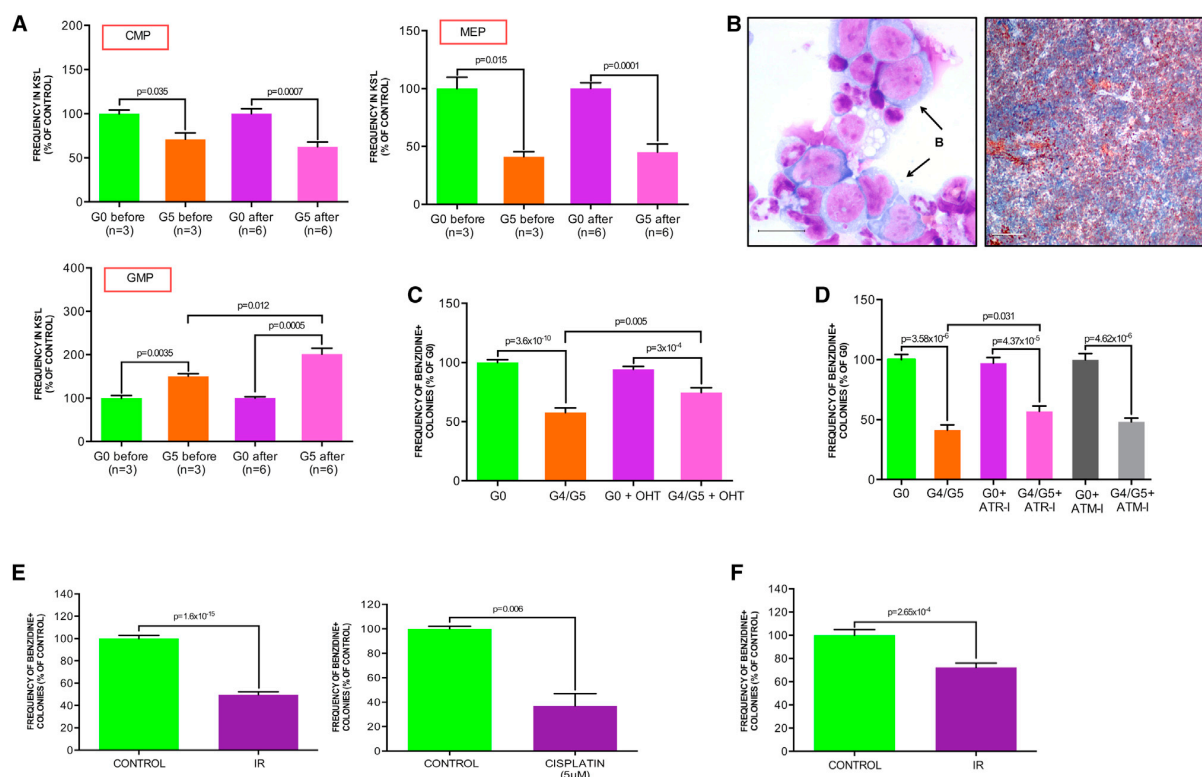


Figure 3. Defective CMP Differentiation Is due to Cell Intrinsic DNA Damage Signaling Activation

(A) CMP, GMP, and MEP frequencies in the KS⁺L population of G0 or G5 mice before and after HSC transplantation in wild-type recipient mice (error bars denote SEM; data are expressed as percentage of corresponding controls).

(B) Representative BM cytopsin of one recipient mouse transplanted with G5 HSCs (on the left). Arrows indicate blastic cells. Massive infiltration of CD11b positive myeloid precursors into the splenic white-red pulp architecture of a recipient mouse transplanted with G5 HSCs (on the right) (the scale bar represents 100 μ m).

(C) Clonogenic myeloid colony formation in methylcellulose from sorted CMP of indicated genotypes cultured in the presence of vehicle or OHT. Erythroid cells were scored by benzidine staining and expressed as frequency of the total number of colonies (mean and SEM of replicates from six experiments of telomerase reactivation in vitro; each experiment includes equal number of CMP sorted from independent mice of indicated genotypes; and data are expressed as percentage of G0 control).

(D) Clonogenic myeloid colony formation in methylcellulose from sorted CMP of indicated genotypes pre-treated with vehicle, ATR inhibitor (ATR-I, 1 micromolar [μ M]), or ATM inhibitor (ATM-I, 2 μ M) for 1 hr. Erythroid cells were scored by benzidine staining and expressed as frequency of the total number of colonies (mean and SEM of replicates from three independent experiments, each experiment includes equal number of CMP sorted from independent mice, and data are expressed as percentage of G0 control).

(E) Clonogenic myeloid colony formation in methylcellulose from sorted wild-type CMP isolated from control or IR (3 Gy) mice (left panel) or pre-treated with vehicle or cisplatin (5 μ M) for 4 hr (right panel). Erythroid cells were scored by benzidine staining and expressed as frequency of the total number of colonies (mean and SEM of replicates from three and two independent experiments, respectively; each experiment includes CMP sorted from a pool of three wild-type mice; and data are expressed as percentage of corresponding controls).

(F) Clonogenic myeloid colony formation in methylcellulose from sorted CMP isolated from 9-month-old wild-type mice 4 months after sub-lethal IR. Control mice indicate age-matched wild-type mice without IR. Erythroid cells were scored by benzidine staining and expressed as frequency of the total number of colonies (mean and SEM of replicates from four or five mice for each condition; equal number of CMP was sorted from independent mice; and data are expressed as percentage of control). See also Figure S3.

the existence of a cell intrinsic telomere dysfunction-induced differentiation checkpoint, which occurs at the level of progenitor cells and contributes to ineffective hematopoiesis, a key feature of the MDS phenotype.

Next, we sought additional evidence to cement the role of DNA damage in altering myeloid differentiation. Employing ionizing radiation and cisplatin treatment as distinct instigators of DNA damage signaling, sorted CMP from wild-type mice subjected

to irradiation (IR, 3 Gy) or cisplatin treatment (5 μ M, 4 hr of cisplatin treatment) show impaired erythroid differentiation (Figure 3E). Notably, skewed myelo-erythroid differentiation occurred even 4 months after sub-lethal IR of wild-type mice (Figure 3F), consistent with recent findings showing that brief exposure to a moderate level of DNA damage is sufficient to maintain chronic DNA damage signaling activation in hematopoietic cells (Insinga et al., 2013).

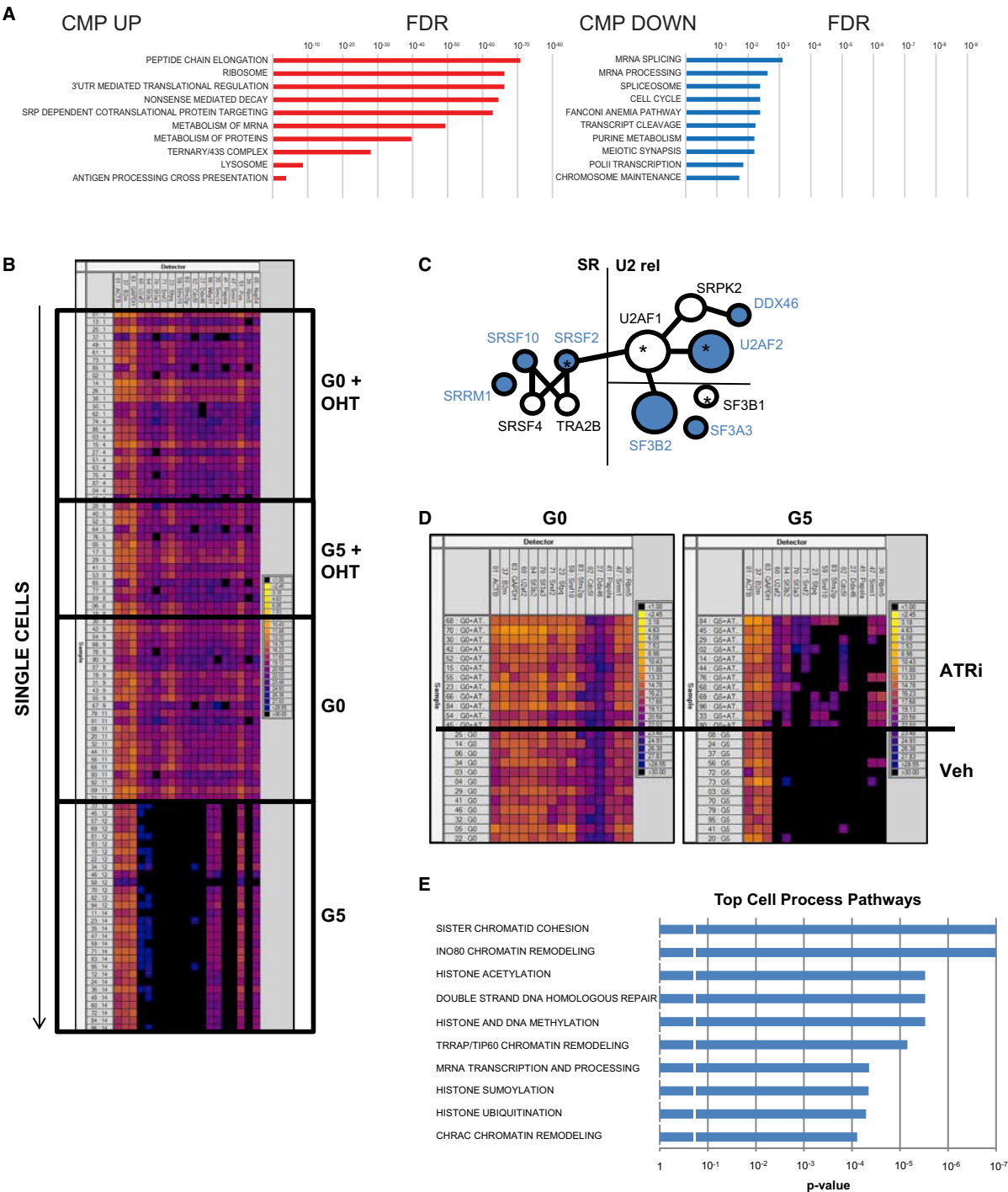


Figure 4. Telomere Dysfunction Induces Aberrant RNA Splicing by Repressing Splicing Gene Expression in CMP

(A) Significantly downregulated and upregulated pathways identified by GSEA in G4/G5 compared to G0 CMP (false discovery rate = 0.05).

(B) Fluidigm-based gene expression analysis of single cells (rows) for representative genes in the mRNA processing/spliceosome pathways (columns) from GSEA, which are significantly altered in sorted CMP from the G0 and G5 mice with or without OHT treatment (n = 3). The genes analyzed were (from left to right): *ACTB*, *β2M*, *GAPDH* (housekeeping genes; internal controls), *U2AF2*, *SF3B2*, *SF3A3*, *SRSF2*, *SFPQ*, *SFRS10*, *SFRS2IP*, *CDC51*, *DDX46*, *WBP11*, *SMC1A*, *PAPOLA*, *SRRM1*, *FUS*, *RBMS*, and *NUP54*. A full gene list is shown in Table S2. The color scale on the right shows correspondence between color code and Ct values. (legend continued on next page)

Telomere Dysfunction Induces Aberrant RNA Splicing by Repressing Splicing Gene Expression in CMP

Next, to determine the mechanistic bases of how telomere dysfunction-induced DNA damage may drive abnormal myeloid differentiation, we performed gene expression profiling analysis of sorted CMP cells from age- and gender-matched G0 or G4/G5 TERT^{ER/ER} mice. Gene set enrichment analysis (GSEA) of the differentially expressed genes of the G4/G5 TERT^{ER/ER} CMP revealed a significant enrichment of genes involved in mRNA splicing and processing (Figure 4A; Table S1), including the splicing factors *U2AF2*, *SRSF2*, *SRSF10*, *SF3B2*, and *SF3A3*. To exclude the possibility that the changes in splicing gene expression were due to cellular heterogeneity in the CMP, we performed single cell Fluidigm real-time PCR and observed a consistent repression of splicing gene expression in every G4/G5 CMP compared to the G0 control (Figure 4B; Table S2), indicating that telomere dysfunction leads to a homogeneous change in splicing gene expression during this particular stage of differentiation. That the splicing pathway was downregulated in the G4/G5 CMP was further validated by western blot analysis (Figure S4A). In striking contrast, the RNA splicing pathway was not altered in the G4/G5 TERT^{ER/ER} GMP (Figure S4B) or MEP (data not shown), a finding which aligns with a lack of a significant γ -H2AX and 53BP1 DNA damage foci increase in these sub-populations (Figures S2E and S2F) and underscores the context-specific impact of DNA damage signaling in the differentiating hematopoietic system. Interestingly, the CMP population also showed preferential and significant downregulation of genes belonging to the cohesin complex (*RAD21*, *STAG1*, *SMC2*, and *SMC5*) (Table S1) that is known to be involved in post-replicative DNA repair (Dorsett and Ström, 2012), and recurrently mutated or deleted in AML and MDS (Kon et al., 2013; Ley et al., 2013), suggesting that DNA damage accumulation in the CMP cells could be further potentiated by the impairment of pathways regulating the DNA damage repair.

We observed an overrepresentation of splicing genes belonging to the same interaction network (Figure 4C), which is known to be involved in the 3' splice site recognition and to play a critical role for commitment complex E formation in U2-dependent splicing or for stabilization of splicing complex A. Remarkably, highly recurrent mutations in some of these same key components of the spliceosome machinery and their interacting partners have been recently reported in MDS (Yoshida et al., 2011), although little is known about how these mutations contribute to the pathogenesis of MDS or its transformation to AML.

To fortify the link between telomere dysfunction-induced DNA damage and suppressed expression of the mRNA splicing and processing components, we quantified the mRNA expression of these genes upon telomerase reactivation and observed that the downregulation of mRNA splicing

and processing components, which was absent in G1 mice (data not shown), was rescued by telomerase reactivation in the G4/G5 mice (Figure 4B). The repression of mRNA splicing and processing components persisted in CMP after the transplantation of telomere dysfunctional HSC in wild-type recipient mice (Figure S4C), establishing that telomere dysfunction-induced DNA damage exerts a prominent cell-intrinsic effect on mRNA splicing regulation. Furthermore, splicing repression in the CMP was significantly rescued when telomere dysfunctional mice were treated with the specific ATR kinase inhibitor VE-821 (Figure 4D), a finding in accord with decreased p-ATR immunofluorescence staining of the CMP after VE-821 treatment (Figure S4D).

Together, these findings indicate that the cell intrinsic telomere dysfunction-induced DNA damage response can impact on the expression of genes involved in splicing regulation through the activation of ATR kinase. In correlative clinical studies, the link between splicing factor expression levels and ATR activation is further supported by a significant correlation between decreased *srsf2* levels and the phosphorylation status of ATR in MDS CD34⁺ cells ($n = 50$, $p = 0.04$, data not shown).

Given that telomere dysfunction results in the downregulation of splicing components, we performed RNA sequencing (RNA-seq) analysis on G0 and G4/G5 TERT^{ER/ER} CMP to assess if the RNA splicing process is indeed altered. Notably, this analysis detected a total of 2,489 aberrant splicing events affecting 1,940 genes in the G4/G5 TERT^{ER/ER} CMP compared to G0 control (Table S3), among which 40.5% and 59.5% of aberrant splicing events would result in exon skipping and exon retention, respectively, consistent with the decreased expression of factors that define the exon-intron boundaries (Figure 4C). Furthermore, we found that 26.9% of aberrant splicing events are predicted to produce loss-of-function transcripts that arise mainly due to a premature stop codon (Table S4) or an in-frame deletion disrupting known functional domains (Table S5). There were no changes in intron retention (data not shown), which we speculate may result from increased expression of genes involved in the nonsense-mediated mRNA decay response present in G4/G5 TERT^{ER/ER} CMP (Zhang and Manley, 2013) (Figure 4A). Of note, the aberrantly spliced transcripts in the G5 CMP population are enriched in pathways that are highly relevant to the MDS phenotype, including the maintenance of genome stability, DNA damage response, chromatin remodeling, and histone modifications (such as acetylation, methylation, sumoylation, and ubiquitination) (Figure 4E).

Epigenetic alterations and histone code changes drive aberrant differentiation of MDS cells, which are sensitive to drugs that modify the epigenome and influence DNA methylation (Issa, 2013). In this regard, it is notable that, among the aberrantly spliced epigenetic regulators in G5 CMP, the protein level of

(C) Interaction network of splicing genes significantly downregulated in G4/G5 CMP (blue color). The size of the nodes is proportional to the number of interactions of a given protein with other splicing components. * indicates splicing factors mutated in MDS.

(D) Fluidigm-based gene expression analysis of single cells (rows) for representative genes in the mRNA processing/spliceosome pathways (columns), which are significantly altered in sorted CMP from the G0 and G5 mice with or without ATR inhibitor treatment ($n = 2$ or 3 mice for each condition). The genes analyzed were (from left to right): *ACTB*, $\beta 2M$, *GAPDH* (housekeeping genes; internal controls), *U2AF2*, *SF3B2*, *SF3A3*, *SRSF2*, *SFPQ*, *SFRS10*, *SFRS2IP*, *CDC51*, *DDX46*, *PAPOLA*, *SRRM1*, and *RBM5*. The color scale on the right shows correspondence between color code and Ct values.

(E) Significantly enriched pathways relative to the 1,940 aberrantly spliced genes ($p < 0.05$). See also Figure S4 and Tables S1, S2, S3, S4, and S5.

DNMT3A DNA methyltransferase decreased due to premature termination of protein translation (Figure S4A) as a result of a frameshift that occurs upon exon skipping (Table S4). In MDS patients, recurrent mutations in *DNMT3A* reduce the methyltransferase activity of the protein and are associated with rapid progression to AML (Walter et al., 2011). Supporting the view that the loss of DNMT3A may impact on DNA methylation, we found locus-specific changes in methylation patterns in the G5 CMP compared to G0 control, involving both gains and losses of methylation in CpG promoters, gene bodies, and intergenic regions (Figures S4E and S4F). These findings are consistent with previous studies showing that DNMT3A loss in the hematopoietic system results in hypo- and hyper-methylation at distinct loci, progressive impairment of differentiation (Challen et al., 2012), and hematological malignancies including MDS (Mayle et al., 2014).

SRSF2 Haploinsufficiency Impairs CMP Differentiation in Mice

Recognizing that an optimal stoichiometry of splicing components is critical for proper spliceosomal function (Cáceres et al., 1994) and that either overexpressing or downregulating particular splicing factors alters splicing activity, we sought multi-level evidence of a causal link between decreased splicing factor activity/expression and abnormal myeloid progenitor differentiation. To that end, we evaluated whether pharmacological or genetic perturbation of the splicing machinery could induce defective myeloid differentiation similar to that observed in the telomere dysfunctional CMP. Using Pladienolide B (PLA-B, a natural macrolide that inhibits the spliceosome assembly through specific Sf3b complex binding, see Kotake et al., 2007), we observed that a transient (4 hr) pre-treatment of sorted wild-type CMP cells prior to differentiation resulted in a profound impairment of differentiation toward the erythroid lineage (Figure S5A). Similar results were obtained with transient NSC663284 treatment that inhibits the catalytic activity of the splicing machinery (Berg et al., 2012) (Figure S5A).

To provide genetic evidence that decreased expression of splicing components impacts progenitor differentiation toward the erythroid lineage, we generated mice heterozygous for *SRSF2* by crossing conditional *SRSF2* knockout mice (*SRSF2*^{L/L}) with hematopoietic cell-specific cre transgenic mice (*Vav-cre*). *SRSF2* is a well-characterized splicing factor involved in both constitutive and regulated splicing (Lin and Fu, 2007) and is significantly downregulated in telomere dysfunctional CMP and recurrently mutated in MDS patients (Yoshida et al., 2011). Although the *Vav-cre/SRSF2*^{L/+} mice showed no obvious hematopoiesis defect in the peripheral blood (data not shown), analysis of the *Vav-cre/SRSF2*^{L/+} BM revealed multi-lineage dysplasia (Figure 5A: hypersegmented neutrophils [20.5% ± 7.76%], erythroblasts [14.75% ± 2.06], and megakaryocytes [27.25% ± 10.93%]), a slight increase in the number of morphological abnormal blasts (Figure 5A: 13% ± 7.57%), and myelomonocytosis (Figure 5B: % of butyrate esterase positive cells is 7% ± 2% in the *Vav-cre* BM versus 16.33% ± 4.67% in the *Vav-cre/SRSF2*^{L/+} BM, *p* = 0.003 and % of CD11b positive cells is 41.66% ± 2.88% in the *Vav-cre* BM versus 67.5% ± 9.57% in the *Vav-cre/SRSF2*^{L/+} BM, *p* = 0.008). Compared to the age- and gender-matched *Vav-cre* controls, the KS⁺L compartment of the

Vav-cre/SRSF2^{L/+} mice showed a slight increase in the frequency of GMP with the concomitant loss of MEP (Figure 5C), which was further confirmed by in vitro methylcellulose clonogenic assay of sorted CMP (Figure 5D).

Aberrant RNA Splicing due to Reduced *SRSF2* Expression Induces Telomere Dysfunction

Next, RNA-seq analysis of *Vav-cre* and *Vav-cre/SRSF2*^{L/+} CMP confirmed altered RNA splicing associated with *SRSF2* haploinsufficiency, detecting 1,682 aberrant splicing events for 1,357 genes (Table S6). Strikingly, these aberrantly spliced genes are involved in telomere maintenance, chromatin remodeling, and DNA repair pathways and show overlap to those genes altered in the telomere dysfunctional CMP (Figure 6A). Consistent with the aberrant splicing and predicted loss-of-function of telomere maintenance genes including *RTEL1* and *TERF2IP* (Figure S6A), *SRSF2* deletion was associated with a significantly increased number of telomere dysfunction-induced foci in the CMP population (Figure 6B) and decreased telomere length in BM cells (Figure 6C). Together, the concordance of RNA splicing profiles of *SRSF2* haploinsufficient and telomerase deficient CMP strongly reinforce the intimate connection between RNA splicing, telomere biology, DNA repair, and MDS phenotype.

Finally, we asked if this functional link was indeed relevant to the human counterpart of MDS, which harbors somatic mutations of spliceosomal genes in over half of all patients (Yoshida et al., 2011). Since CMML patients are also characterized by skewed myeloid differentiation toward the myelo-monocytic lineage and present high rate of *SRSF2* mutation (hence potentially affecting RNA splicing) (Itzykson et al., 2013), we evaluated *SRSF2* mutation (P95)-specific exon usage patterns by RNA-seq analysis of *SRSF2* mutant (*n* = 6) and wild-type (*n* = 9) CD34⁺ cells isolated from CMML patients, to understand the functional consequences of *SRSF2* mutation on RNA processing/splicing. This analysis detected a total of 1,536 aberrant splicing events affecting 1,355 genes (Table S7), mainly involved in DNA repair and telomere maintenance pathways (Figure 6D), which overlapped with the telomere dysfunctional (Figure 4E) and *SRSF2* haploinsufficient CMP RNA-seq data sets (Figure 6A). Specifically, we found that transcripts encoding ACD, which is a component of the shelterin telomeric complex, and TNKS, which interacts with TRF1, to be aberrantly spliced in CD34⁺ cells with *SRSF2* mutation, with predicted loss of function of these telomere maintenance genes. Together, these findings strongly support the view that perturbation of RNA splicing either through loss of *SRSF2* expression or *SRSF2* mutation results in the aberrant splicing of a specific subset of genes, including those that influence telomere dynamics, which is predicted to induce telomere dysfunction and exacerbate aberrant RNA splicing.

DISCUSSION

Our study provides multi-level evidence that telomere dysfunction can be a critical factor driving MDS and that diminished splicing factor expression induced by telomere dysfunction drives myeloid differentiation processes in a manner that contributes to the high risk MDS phenotype. On the mechanistic level, genetic, pharmacological, and correlative clinical data establish that telomere dysfunction represses the expression

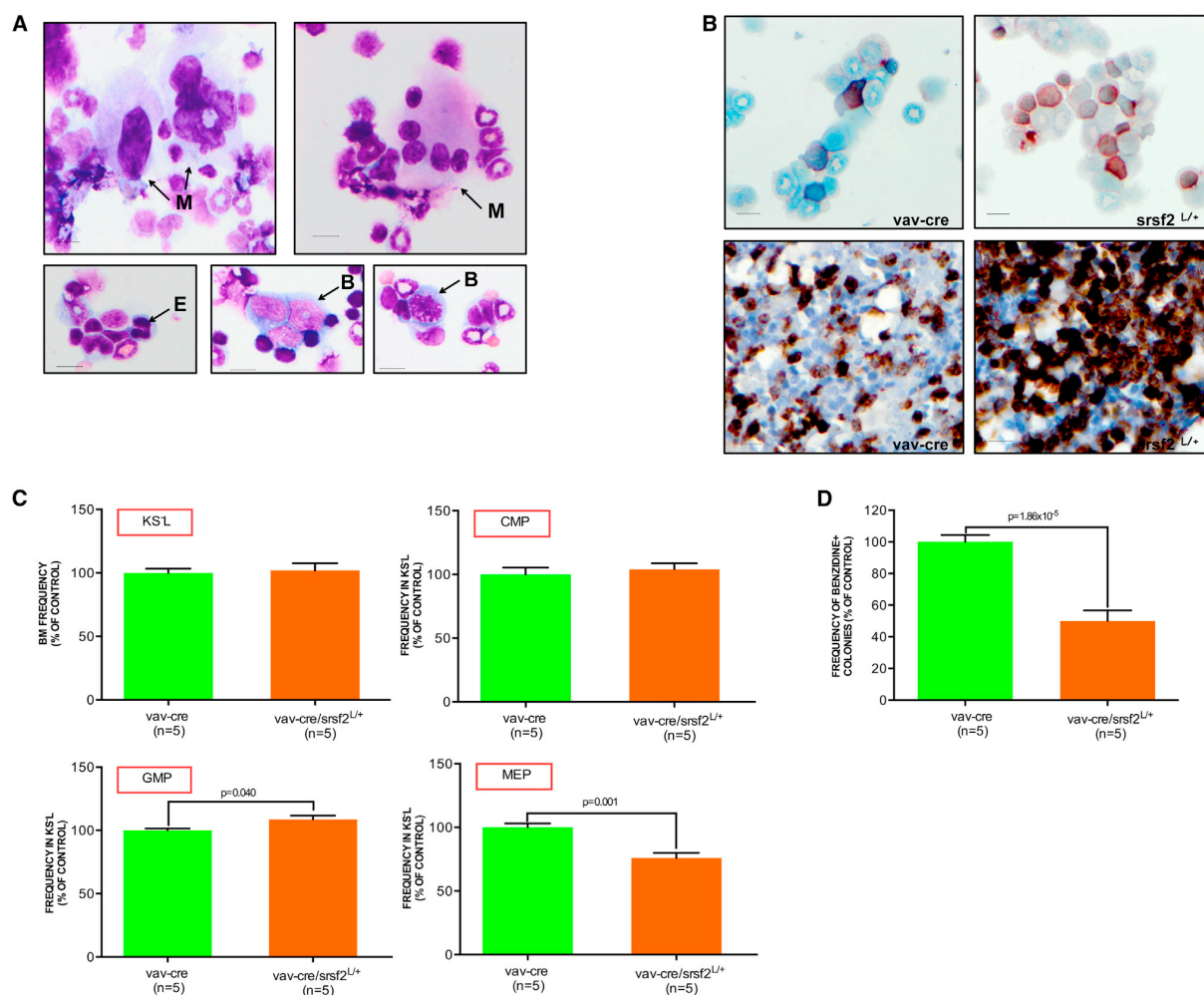


Figure 5. SRSF2 Haploinsufficiency Induces Skewed Myeloid Differentiation of CMP

(A) Dysplastic monolobated and hyperlobated (upper panel, on the left) or multi-nucleated (upper panel, on the right) megakaryocytes (M), dysplastic erythroblast (E, bottom left) and abnormal (bottom panel, in the middle), and mitotic (bottom panel, on the right) blasts (B) in a representative *Vav-cre/SRSF2^{L/+}* BM cytopsin (the scale bar represents 15 μ m).

(B) Butyrate esterase cytochemical staining of a representative *Vav-cre* (upper panel, on the left) or *Vav-cre/SRSF2^{L/+}* BM cytopsin (upper panel, on the right). CD11b stained sections of BM biopsies of representative *Vav-cre* (bottom panel on the left) and *Vav-cre/SRSF2^{L/+}* (bottom panel on the right) mice (the scale bar represents 15 μ m).

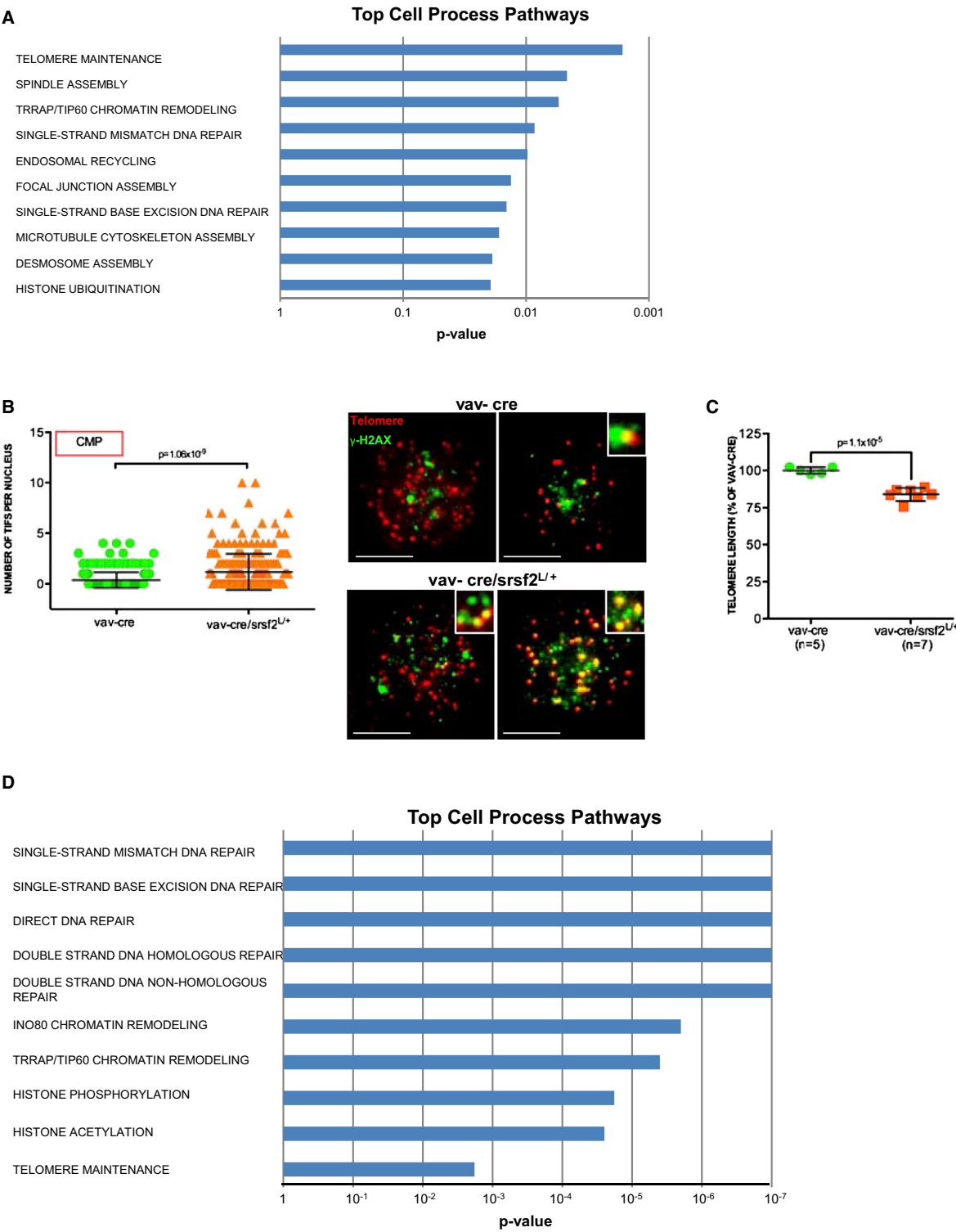
(C) KSL frequency in the BM, as well as the CMP, GMP, and MEP frequencies in the KSL compartment of 2-month-old *Vav-cre* (n = 5) or *Vav-cre/SRSF2^{L/+}* (n = 5) mice (error bars denote SEM; data are expressed as percentage of the *Vav-cre* control).

(D) Clonogenic myeloid colony formation in methylcellulose from CMP sorted from *Vav-cre* or *Vav-cre/SRSF2^{L/+}* mice. Erythroid cells were scored by benzidine staining and expressed as frequency of the total number of colonies (mean and SEM of replicates from five independent mice; data are expressed as percentage of *Vav-cre* control). See also Figure S5.

of genes governing RNA splicing in part through ATR. Notably, on the clinical level, increased p-ATR staining is strongly correlated with high risk MDS in patients, a finding of therapeutic clinical utility in the prevention and treatment of aging-associated or therapy-induced MDS.

An unexpected finding from our study is the highly specific impact of telomere dysfunction and DNA damage on progenitor differentiation and RNA splicing. We propose that accumulating levels of physiological DNA damage perturb RNA splicing and

thus impair the differentiation of specific progenitor sub-populations, possibly via de-regulation of epigenetic and DNA repair factors. This is consistent with previous studies which have demonstrated that genetic alterations in DNA repair genes can result in BM failure syndromes and familial MDS by altering differentiation of hematopoietic cells (Geiselhart et al., 2012; Owen et al., 2008). Furthermore, it is tempting to speculate that defective DNA repair in these progenitors may also fuel secondary events that predispose to AML transformation. This may



(legend on next page)

be of considerable relevance for the disease progression and subsequent AML transformation that is frequently seen in MDS patients and is consistent with the view that leukemic stem cells often display a progenitor rather than a stem cell phenotype in AML (Goardon et al., 2011).

Through pharmacologic and genetic perturbation of RNA splicing, we provided evidence that aberrant RNA splicing alone impairs CMP differentiation, supporting the view that aberrant RNA splicing upon telomere dysfunction is one of the mechanisms underlying the skewed myeloid differentiation (and MDS phenotypes) seen in vivo. Indeed, reduced *SRSF2* expression in the *Vav-cre/ SRSF2^{L/+}* mouse model partially recapitulates the MDS features observed in the telomere dysfunctional mice. An unanticipated finding is that both *SRSF2* haploinsufficiency and *SRSF2* mutation resulted in the aberrant splicing of genes that are involved in telomere maintenance, DNA repair, and chromatin remodeling—pathways extremely relevant to MDS pathogenesis—which are also altered in the telomere dysfunctional CMP as a consequence of DNA damage-induced downregulation of splicing factor expression. Furthermore, our observation that splicing de-regulation induces telomere dysfunction underscores a connection between RNA splicing and telomere biology, which warrants further investigation.

Despite significant convergence of pathways with mutant *SRSF2* and *SRSF2* haploinsufficiency, we also observed differences in the aberrantly spliced transcripts, suggesting that the process of RNA splicing is executed differentially with *SRSF2* mutation compared to its loss of function (e.g., different splice site recognition), which may explain the weaker MDS phenotype observed in *Vav-cre/ SRSF2^{L/+}* mice. This observation concurs with what has been shown for the splicing gene *PRPF8* (Kurtovic-Kozaric et al., 2014) and is consistent with many other examples of cancer relevant genes, such as the *TP53* tumor suppressor gene, whereby *TP53* deletion and *TP53* mutation share many commonalities in cancer pathogenesis, but are not identical in function (Lang et al., 2004).

In conclusion, our studies reveal an intimate relationship between telomeres and mRNA splicing in the control of cellular differentiation of specific hematopoietic cell sub-populations, but the molecular details are still to be clarified. We propose that telomere dysfunction causes aberrant RNA splicing (by downregulating splicing factors), which exacerbates telomere erosion (by aberrantly splicing of telomere maintenance genes), impairing progenitor cell differentiation, culminating in the eventual progression to AML. Our results are consistent with the long-standing clinical observations that poor prognosis in MDS correlates strongly with short telomeres and elevated DNA damage accumulation in myeloid progenitor cells and that therapy-related MDS can result from cancer treatments utilizing alkylating agents or ionizing radiations. The improved understanding

of DNA-damage induced perturbations in the splicing of specific transcripts and linked pathways reported here should provide highly specific risk biomarkers and therapeutic targets for the prevention or treatment of this incurable disease.

EXPERIMENTAL PROCEDURES

Generation and Analysis of Mice

Mice were maintained in specific pathogen-free (SPF) conditions at MD Anderson Cancer Center. All manipulations were performed with institutional animal care and use committee (IACUC) approval. The heterozygous (G0 *TERT^{ER/+}*) and late generation homozygous (G4/G5 *TERT^{ER/ER}*) mice were generated based on standard breeding protocol of successive generations of telomerase-deficient mice (Jaskelioff et al., 2011). All studies were performed on adult (12–16 week old) G0 *TERT^{ER/+}* and telomere dysfunctional G4/G5 *TERT^{ER/ER}* mice, unless otherwise noted. OHT time-release pellets (2.5 milligrams [mg]; Innovative Research of America) were inserted subcutaneously to reach steady-state blood levels of 1 nanogram (ng) milliliter (ml)^{−1} OHT. The conditional deletion of *SRSF2* in the hematopoietic compartment was accomplished by crossing *Vav-cre* mice (Jackson laboratories) with the *srsf2^{L/L}* mice (Jackson laboratories) to generate heterozygous *Vav-cre/ SRSF2^{L/+}* mice. Animals were autopsied, and the BM and spleen tissues were examined regardless of their pathological status. Details are described in [Supplemental Experimental Procedures](#).

Human Primary Samples

Human MDS or CMML BM specimens were obtained from patients referred to the Department of Leukemia at MD Anderson Cancer Center following protocol LAB01-473, which was approved by MD Anderson's Institutional Review Board. Written informed consent was obtained from donors. MDS BM cells were collected from 57 MDS and 15 CMML patients. Diagnosis was confirmed by a dedicated hematopathologist and patients were classified as lower or higher risk MDS according to the International Prognostic Scoring System (IPSS). Isolation of CD34⁺ cells was performed using MicroBead Kit (Miltenyi), following manufacturer's instructions. An aliquot of purified CD34⁺ cells was used to prepare cytospin slides; the remainder was subjected to centrifugation at 300 × g for 10 min and resuspended in TRIzol (Invitrogen) for RNA extraction.

Flow Cytometry Analysis

Single-cell suspensions were prepared from spleen and BM (from femoral and tibial bones). For fluorescence-activated cell sorter (FACS) sorting and analysis, we used described staining protocols and published stem and progenitor cell definitions (Amrani et al., 2011; Flach et al., 2014). Details are described in [Supplemental Experimental Procedures](#).

Indirect Immunofluorescence Microscopy and Tif Assay

Sorted progenitor cells were resuspended in PBS, spotted on immunofluorescence slides, fixed, and immuno-stained with anti-phospho-γH2AX (1:200; clone number JBW301, Millipore), 53BP1 (1:200, catalog number IHC00001, Bethyl Laboratories), or phospho-ATR (1:50; catalog number 2853, Cell Signaling). For Tif assay, cells were co-stained with phospho-H2AX and the telomere specific PNA probe using the Telomere PNA FISH Kit/Cy3, according to the manufacturer's instructions. Details are described in [Supplemental Experimental Procedures](#).

Figure 6. Aberrant RNA Splicing due to Altered *SRSF2* Function Induces Telomere Dysfunction

- (A) Significantly enriched pathways relative to the 1,357 aberrantly spliced genes ($p < 0.05$) in the *Vav-cre/ SRSF2^{L/+}* mice.
 (B) Telomere-FISH and anti-γH2AX immunofluorescence in CMP sorted from 5-month-old mice of indicated genotypes (telomere: red; anti-γH2AX: green; co-localization: yellow; and $n = 5$ *Vav-cre* and $n = 7$ *Vav-cre/ SRSF2^{L/+}*); numbers of telomere dysfunction-induced foci per cell (left panel) (error bars denote SEM); and representative images (right panel) (the scale bar represents 10 μm).
 (C) Mean value of telomere length in primary BM cells of 5-month-old mice of indicated genotypes, as determined by flow-FISH analysis (error bars denote SEM; data are expressed as percentage of the *Vav-cre* control).
 (D) Significantly enriched pathways relative to the 1,355 aberrantly spliced genes ($p < 0.01$) in CMML patients with *SRSF2* (P95) mutation. See also [Figure S6](#) and [Tables S6](#) and [S7](#).

Treatments and Colony Forming Assay

MNCs (20×10^4 /replicate) or sorted CMP (500 cells/replicate) were seeded into cytokine supplemented methylcellulose medium or pre-treated with a specific inhibitor of ATR, ATM, cisplatin, PLA-B, or NSC663284 prior to seeding. Colonies were counted after 7–10 days. Erythroid cells were scored by benzidine staining. Details are described in [Supplemental Experimental Procedures](#).

Microarray and Pathway Analysis

BM, CMP, and GMP cells were sorted from two paired pools of G0 TERT^{ER/+} or G4/G5 TERT^{ER/ER} mice (5,000–20,000 cells per sample) and RNA was extracted using TRIzol. Gene expression profiling was performed with GeneChip Mouse Genome 430 2.0 Array (Affymetrix) and enriched pathways were identified using GSEA (<http://www.broadinstitute.org/gsea/msigdb/annotate.jsp>). Details are described in [Supplemental Experimental Procedures](#).

Single-Cell Gene Expression Profiling

Single CMP cells were sorted directly into 96-well plates before Fluidigm-based real-time PCR analysis. Details are described in [Supplemental Experimental Procedures](#).

RNA-Seq and Analysis

Total RNA from sorted CMP isolated from three independent G0 TERT^{ER/+} and four G4/G5 TERT^{ER/ER}, three *Vav-cre*, and six *Vav-cre/Srsf2^{L/+}* mice, as well as CML patient-derived CD34⁺ cells ($n = 15$) were isolated by TRIzol, before RNA amplification and RNA-seq library construction. Transcriptomic sequencing (RNA-seq) was performed on the Illumina HiSeq platform using the standard paired-end protocol. Mapping of RNA-seq reads was performed with Tophat2 and the National Center for Biotechnology Information (NCBI) RefSeq gene model and HTSeq software were used to quantify the gene-level expression, exon-specific expression, and intron retention levels. The differential analyses for gene/isoform expression and intron retention were analyzed with DESeq2 ([Anders and Huber, 2010](#)), while exon usage was analyzed with DEXSeq ([Anders et al., 2012](#)). Pathway enrichment analysis was performed with Pathway Studio. Details are described in [Supplemental Experimental Procedures](#).

Western Blotting

Western blotting in small amount of cells was performed as previously described ([Nakada et al., 2010](#)). Antibodies were anti-sfrs2 (clone number 1SC-4F11, Millipore), anti-sf3b2 (clone number 5D2, Sigma), anti-dnmt3a (clone number H-295, Santa Cruz), anti-terf2ip (clone number D9H4, Cell Signaling), and anti-vinculin (clone number hVIN-1, Sigma). Details are described in [Supplemental Experimental Procedures](#).

BM Transplantations

Donor derived peripheral blood reconstitution (i.e., chimerism) was assessed after 2 or 4 months following transplantation by FACS analysis of nucleated peripheral blood cells stained with anti-CD45.1 and anti-CD45.2-specific antibodies. Blood chimerism for each recipient was calculated as the percentage of all CD45⁺ cells that were CD45.2⁺. Details are described in [Supplemental Experimental Procedures](#).

Statistical Analysis

All the data were analyzed by a two-tailed Student's *t* test ($p < 0.05$ is considered to be statistically significant). For all experiments with error bars, SEM was calculated to indicate the variation within each experiment and data, and values represent mean \pm SEM or mean \pm SD, as indicated in the figure legends.

ACCESSION NUMBERS

All data sets generated in this study using Microarray and RBBS are now accessible at GEO under GSE62393, while RNA-seq is accessible at ftp://ftp.ncbi.nih.gov/pub/TraceDB/misc/tmp/SRP048846_SRP048858.

SUPPLEMENTAL INFORMATION

Supplemental Information includes Supplemental Experimental Procedures, six figures, and seven tables and can be found with this article online at <http://dx.doi.org/10.1016/j.ccell.2015.04.007>.

AUTHOR CONTRIBUTION

S.C., D.S.T.O., G.G.-M., and R.A.D. designed and guided the research; and S.C., D.S.T.O., Y.O., A.V., P.S., Y.A.W., H.Y., D.C.W., N.G., S.H., Y.W.H., B.H., G.G., P.P., S.J., A.C., L.N., M.D.A., and I.G.-G. performed research. M.M. performed and analyzed immunofluorescence experiments. N.A.M., M.C.R., L.Z., and H.L. analyzed RNA-seq data. S.A.A. performed and analyzed Fluidigm experiments. K.C.-D. and K.R. analyzed flow cytometry data. C.A.B. analyzed microarray data. A.S.M. performed cytogenetic analysis. M.E., S.G., and T.G. analyzed methylation data. C.B.-R. performed cytochemical and histological analyses. J.W.H., T.P.H., P.J., H.K., L.J.N.C., Y.A.W., and L.C. provided critical intellectual contributions throughout the project. S.C., D.S.T.O., and R.A.D. wrote the manuscript.

ACKNOWLEDGMENTS

We thank all members of the DePinho, Chin, and Draetta laboratories for fruitful suggestions and discussions. This work is supported by the National Cancer Institute (NCI) (R01 CA084628 to R.A.D. and MD Anderson TCGA Genome Data Analysis Center, grant number CA143883). D.S.T.O. is an Odyssey Fellow at MD Anderson Cancer Center and supported by the Laura and John Arnold Foundation. Flow cytometry was done with the assistance of the South Campus Flow Cytometry and Cell Sorting Core Laboratory, which is supported in part by NIH P30 CA16672. Dr. Cooper has patents with Sangamo BioSciences with artificial nucleases. He consults with Targazyme, Inc. (formerly American Stem Cells, Inc.) and receives compensation. He also consults with GE Healthcare and Ferring Pharmaceuticals. He receives honoraria from Miltenyi Biotec. He has licensed technology to Intrexon and Ziopharm and receives compensation.

Received: December 23, 2014

Revised: January 31, 2015

Accepted: April 13, 2015

Published: May 11, 2015

REFERENCES

- Akashi, K., Traver, D., Miyamoto, T., and Weissman, I.L. (2000). A clonogenic common myeloid progenitor that gives rise to all myeloid lineages. *Nature* 404, 193–197.
- Allsopp, R.C., Morin, G.B., DePinho, R., Harley, C.B., and Weissman, I.L. (2003). Telomerase is required to slow telomere shortening and extend replicative lifespan of HSCs during serial transplantation. *Blood* 102, 517–520.
- Amrani, Y.M., Gill, J., Matevosian, A., Alonzo, E.S., Yang, C., Shieh, J.H., Moore, M.A., Park, C.Y., Sant'Angelo, D.B., and Denzin, L.K. (2011). The *Paf* oncogene is essential for hematopoietic stem cell function and development. *J. Exp. Med.* 208, 1757–1765.
- Anders, S., and Huber, W. (2010). Differential expression analysis for sequence count data. *Genome Biol.* 11, R106.
- Anders, S., Reyes, A., and Huber, W. (2012). Detecting differential usage of exons from RNA-seq data. *Genome Res.* 22, 2008–2017.
- Bejar, R., Stevenson, K., Abdel-Wahab, O., Galili, N., Nilsson, B., Garcia-Manero, G., Kantarjian, H., Raza, A., Levine, R.L., Neuberg, D., and Ebert, B.L. (2011). Clinical effect of point mutations in myelodysplastic syndromes. *N. Engl. J. Med.* 364, 2496–2506.
- Berg, M.G., Wan, L., Younis, I., Diem, M.D., Soo, M., Wang, C., and Dreyfuss, G. (2012). A quantitative high-throughput in vitro splicing assay identifies inhibitors of spliceosome catalysis. *Mol. Cell. Biol.* 32, 1271–1283.

- Cáceres, J.F., Stamm, S., Helfman, D.M., and Krainer, A.R. (1994). Regulation of alternative splicing in vivo by overexpression of antagonistic splicing factors. *Science* 265, 1706–1709.
- Challen, G.A., Sun, D., Jeong, M., Luo, M., Jelinek, J., Berg, J.S., Bock, C., Vasanthakumar, A., Gu, H., Xi, Y., et al. (2012). Dnmt3a is essential for hematopoietic stem cell differentiation. *Nat. Genet.* 44, 23–31.
- Chin, L., Artandi, S.E., Shen, Q., Tam, A., Lee, S.L., Gottlieb, G.J., Greider, C.W., and DePinho, R.A. (1999). p53 deficiency rescues the adverse effects of telomere loss and cooperates with telomere dysfunction to accelerate carcinogenesis. *Cell* 97, 527–538.
- d'Adda di Fagnana, F., Reaper, P.M., Clay-Farrace, L., Fiegler, H., Carr, P., Von Zglinicki, T., Saretzki, G., Carter, N.P., and Jackson, S.P. (2003). A DNA damage checkpoint response in telomere-initiated senescence. *Nature* 426, 194–198.
- Dorsett, D., and Ström, L. (2012). The ancient and evolving roles of cohesin in gene expression and DNA repair. *Curr. Biol.* 22, R240–R250.
- Flach, J., Bakker, S.T., Mohrin, M., Conroy, P.C., Pietras, E.M., Reynaud, D., Alvarez, S., Diolaiti, M.E., Ugarte, F., Forsberg, E.C., et al. (2014). Replication stress is a potent driver of functional decline in ageing haematopoietic stem cells. *Nature* 512, 198–202.
- Geiselhart, A., Lier, A., Walter, D., and Milsom, M.D. (2012). Disrupted signaling through the Fanconi anemia pathway leads to dysfunctional hematopoietic stem cell biology: underlying mechanisms and potential therapeutic strategies. *Anemia*. <http://dx.doi.org/10.1155/2012/265790>.
- Goardon, N., Marchi, E., Atzberger, A., Quek, L., Schuh, A., Soneji, S., Woll, P., Mead, A., Alford, K.A., Rout, R., et al. (2011). Coexistence of LMPP-like and GMP-like leukemia stem cells in acute myeloid leukemia. *Cancer Cell* 19, 138–152.
- Insinga, A., Cicalese, A., Faretta, M., Gallo, B., Albano, L., Ronzoni, S., Furia, L., Viale, A., and Pelicci, P.G. (2013). DNA damage in stem cells activates p21, inhibits p53, and induces symmetric self-renewing divisions. *Proc. Natl. Acad. Sci. USA* 110, 3931–3936.
- Issa, J.P. (2013). The myelodysplastic syndrome as a prototypical epigenetic disease. *Blood* 121, 3811–3817.
- Itzykson, R., Kosmider, O., Renneville, A., Morabito, M., Preudhomme, C., Berthon, C., Adès, L., Fenaux, P., Platzbecker, U., Gagey, O., et al. (2013). Clonal architecture of chronic myelomonocytic leukemias. *Blood* 121, 2186–2198.
- Jaskelioff, M., Muller, F.L., Paik, J.H., Thomas, E., Jiang, S., Adams, A.C., Sahin, E., Kost-Alimova, M., Protopopov, A., Cadiñanos, J., et al. (2011). Telomerase reactivation reverses tissue degeneration in aged telomerase-deficient mice. *Nature* 469, 102–106.
- Ju, Z., Jiang, H., Jaworski, M., Rathinam, C., Gompf, A., Klein, C., Trumpp, A., and Rudolph, K.L. (2007). Telomere dysfunction induces environmental alterations limiting hematopoietic stem cell function and engraftment. *Nat. Med.* 13, 742–747.
- Karlseder, J., Smogorzewska, A., and de Lange, T. (2002). Senescence induced by altered telomere state, not telomere loss. *Science* 295, 2446–2449.
- Kastan, M.B., and Bartek, J. (2004). Cell-cycle checkpoints and cancer. *Nature* 432, 316–323.
- Kon, A., Shih, L.Y., Minamino, M., Sanada, M., Shiraishi, Y., Nagata, Y., Yoshida, K., Okuno, Y., Bando, M., Nakato, R., et al. (2013). Recurrent mutations in multiple components of the cohesin complex in myeloid neoplasms. *Nat. Genet.* 45, 1232–1237.
- Kotake, Y., Sagane, K., Owa, T., Mimori-Kiyosue, Y., Shimizu, H., Uesugi, M., Ishihama, Y., Iwata, M., and Mizui, Y. (2007). Splicing factor SF3b as a target of the antitumor natural product pladienolide. *Nat. Chem. Biol.* 3, 570–575.
- Kurtovic-Kozaric, A., Przychodzen, B., Singh, J., Konarska, M.M., Clemente, M.J., Otrrock, Z.K., Nakashima, M., Hsi, E.D., Yoshida, K., Shiraishi, Y., et al. (2014). PRPF8 defects cause missplicing in myeloid malignancies. *Leukemia* 29, 126–136.
- Lang, G.A., Iwakuma, T., Suh, Y.A., Liu, G., Rao, V.A., Parant, J.M., Valentin-Vega, Y.A., Terzian, T., Caldwell, L.C., Strong, L.C., et al. (2004). Gain of function of a p53 hot spot mutation in a mouse model of Li-Fraumeni syndrome. *Cell* 119, 861–872.
- Larsson, C.A., Cote, G., and Quintás-Cardama, A. (2013). The changing mutational landscape of acute myeloid leukemia and myelodysplastic syndrome. *Mol. Cancer Res.* 11, 815–827.
- Lee, H.W., Blasco, M.A., Gottlieb, G.J., Horner, J.W., 2nd, Greider, C.W., and DePinho, R.A. (1998). Essential role of mouse telomerase in highly proliferative organs. *Nature* 392, 569–574.
- Ley, T.J., Miller, C., Ding, L., Raphael, B.J., Mungall, A.J., Robertson, A.G., Hoadley, K., Triche, T.J., Laird, P.W., Baty, J.D., et al.; Cancer Genome Atlas Research Network (2013). Genomic and epigenomic landscapes of adult de novo acute myeloid leukemia. *N. Engl. J. Med.* 368, 2059–2074.
- Lin, S., and Fu, X.D. (2007). SR proteins and related factors in alternative splicing. *Adv. Exp. Med. Biol.* 623, 107–122.
- Mayle, A., Yang, L., Rodriguez, B., Zhou, T., Chang, E., Curry, C.V., Challen, G.A., Li, W., Wheeler, D., Rebel, V.I., et al. (2014). Dnmt3a loss predisposes murine hematopoietic stem cells to malignant transformation. *Blood* 125, 629–638.
- Milyavsky, M., Gan, O.I., Trottier, M., Komosa, M., Tabach, O., Notta, F., Lechman, E., Hermans, K.G., Eppert, K., Kononova, Z., et al. (2010). A distinctive DNA damage response in human hematopoietic stem cells reveals an apoptosis-independent role for p53 in self-renewal. *Cell Stem Cell* 7, 186–197.
- Nakada, D., Saunders, T.L., and Morrison, S.J. (2010). Lkb1 regulates cell cycle and energy metabolism in hematopoietic stem cells. *Nature* 468, 653–658.
- Owen, C., Barnett, M., and Fitzgibbon, J. (2008). Familial myelodysplasia and acute myeloid leukaemia—a review. *Br. J. Haematol.* 140, 123–132.
- Pang, W.W., Pluvinage, J.V., Price, E.A., Sridhar, K., Arber, D.A., Greenberg, P.L., Schrier, S.L., Park, C.Y., and Weissman, I.L. (2013). Hematopoietic stem cell and progenitor cell mechanisms in myelodysplastic syndromes. *Proc. Natl. Acad. Sci. USA* 110, 3011–3016.
- Rollison, D.E., Howlader, N., Smith, M.T., Strom, S.S., Merritt, W.D., Ries, L.A., Edwards, B.K., and List, A.F. (2008). Epidemiology of myelodysplastic syndromes and chronic myeloproliferative disorders in the United States, 2001–2004, using data from the NAACCR and SEER programs. *Blood* 112, 45–52.
- Rossi, D.J., Bryder, D., Seita, J., Nussenzweig, A., Hoeijmakers, J., and Weissman, I.L. (2007). Deficiencies in DNA damage repair limit the function of haematopoietic stem cells with age. *Nature* 447, 725–729.
- Rudolph, K.L., Chang, S., Lee, H.W., Blasco, M., Gottlieb, G.J., Greider, C., and DePinho, R.A. (1999). Longevity, stress response, and cancer in aging telomerase-deficient mice. *Cell* 96, 701–712.
- Sahin, E., and DePinho, R.A. (2012). Axis of ageing: telomeres, p53 and mitochondria. *Nat. Rev. Mol. Cell Biol.* 13, 397–404.
- Walter, M.J., Ding, L., Shen, D., Shao, J., Grillot, M., McLellan, M., Fulton, R., Schmidt, H., Kalicki-Veizer, J., O'Laughlin, M., et al. (2011). Recurrent DNMT3A mutations in patients with myelodysplastic syndromes. *Leukemia* 25, 1153–1158.
- Wang, J., Sun, Q., Morita, Y., Jiang, H., Gross, A., Lechel, A., Hildner, K., Guachalla, L.M., Gompf, A., Hartmann, D., et al. (2012). A differentiation checkpoint limits hematopoietic stem cell self-renewal in response to DNA damage. *Cell* 148, 1001–1014.
- Will, B., Zhou, L., Vogler, T.O., Ben-Neriah, S., Schinke, C., Tamari, R., Yu, Y., Bhagat, T.D., Bhattacharyya, S., Barreyro, L., et al. (2012). Stem and progenitor cells in myelodysplastic syndromes show aberrant stage-specific expansion and harbor genetic and epigenetic alterations. *Blood* 120, 2076–2086.
- Yamamoto, R., Morita, Y., Ooehara, J., Hamanaka, S., Onodera, M., Rudolph, K.L., Ema, H., and Nakauchi, H. (2013). Clonal analysis unveils self-renewing lineage-restricted progenitors generated directly from hematopoietic stem cells. *Cell* 154, 1112–1126.
- Yoshida, K., Sanada, M., Shiraishi, Y., Nowak, D., Nagata, Y., Yamamoto, R., Sato, Y., Sato-Otsubo, A., Kon, A., Nagasaki, M., et al. (2011). Frequent pathway mutations of splicing machinery in myelodysplasia. *Nature* 478, 64–69.
- Zhang, J., and Manley, J.L. (2013). Misregulation of pre-mRNA alternative splicing in cancer. *Cancer Discov.* 3, 1228–1237.
- Zhou, T., Hasty, P., Walter, C.A., Bishop, A.J.R., Scott, L.M., and Rebel, V.I. (2013). Myelodysplastic syndrome: an inability to appropriately respond to damaged DNA? *Exp. Hematol.* 41, 665–674.

Supplemental Information

Telomere Dysfunction Drives Aberrant Hematopoietic Differentiation and Myelodysplastic Syndrome

Simona Colla, Derrick Sek Tong Ong, Yamini Ogoti, Matteo Marchesini, Nipun A. Mistry, Karen Clise-Dwyer, Sonny A. Ang, Paola Storti, Andrea Viale, Nicola Giuliani, Kathryn Ruisaard, Irene Ganan Gomez, Christopher A. Bristow, Marcos Estecio, David C. Weksberg, Yan Wing Ho, Baoli Hu, Giannicola Genovese, Piergiorgio Pettazzoni, Asha S. Multani, Shan Jiang, Sujun Hua, Michael C. Ryan, Alessandro Carugo, Luigi Nezi, Yue Wei, Hui Yang, Marianna D'Anca, Li Zhang, Sarah Gaddis, Ting Gong, James W. Horner, Timothy P. Heffernan, Philip Jones, Laurence J.N. Cooper, Han Liang, Hagop Kantarjian, Y. Alan Wang, Lynda Chin, Carlos Bueso-Ramos, Guillermo Garcia-Manero, and Ronald A. DePinho

SUPPLEMENTAL DATA

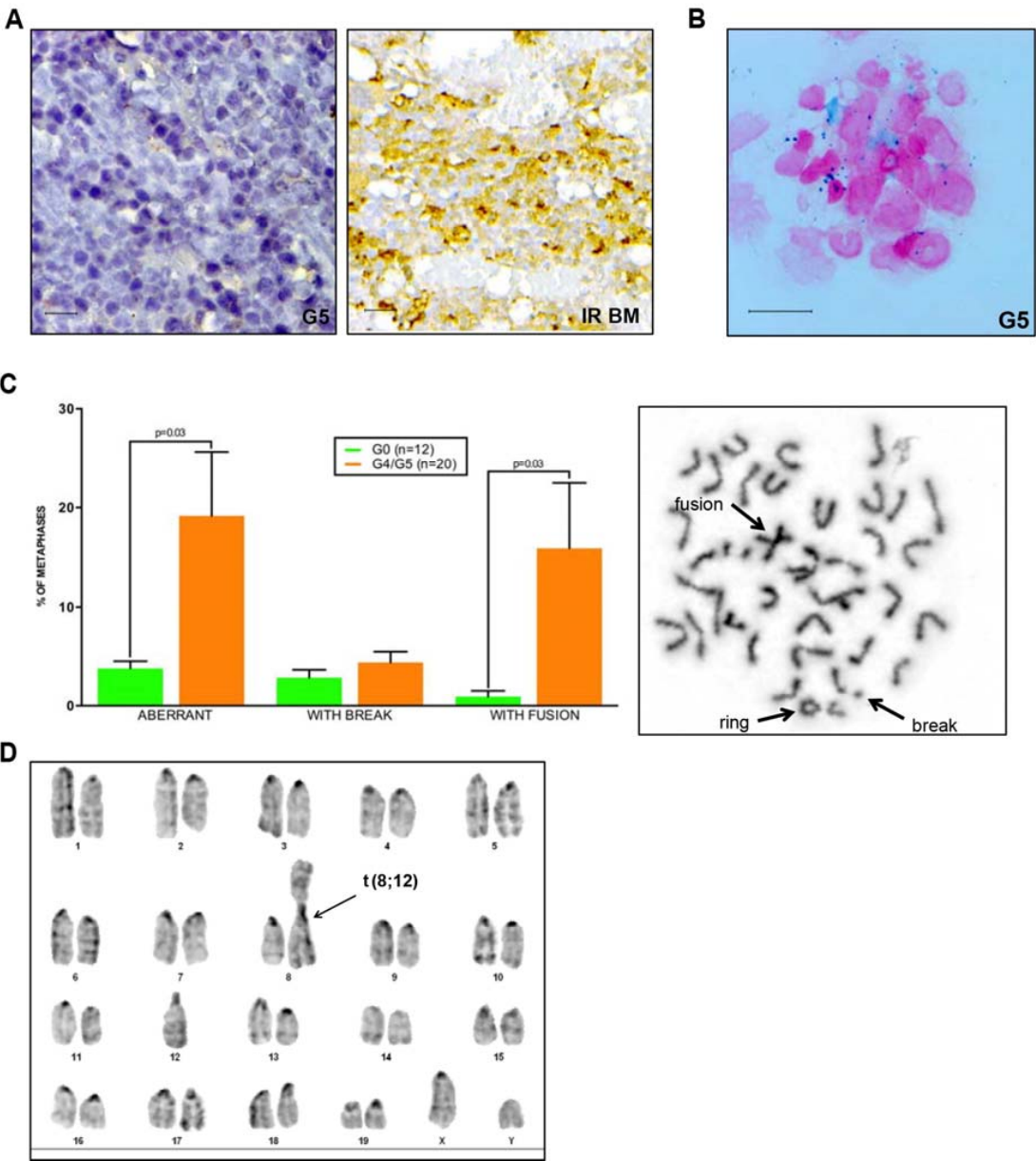


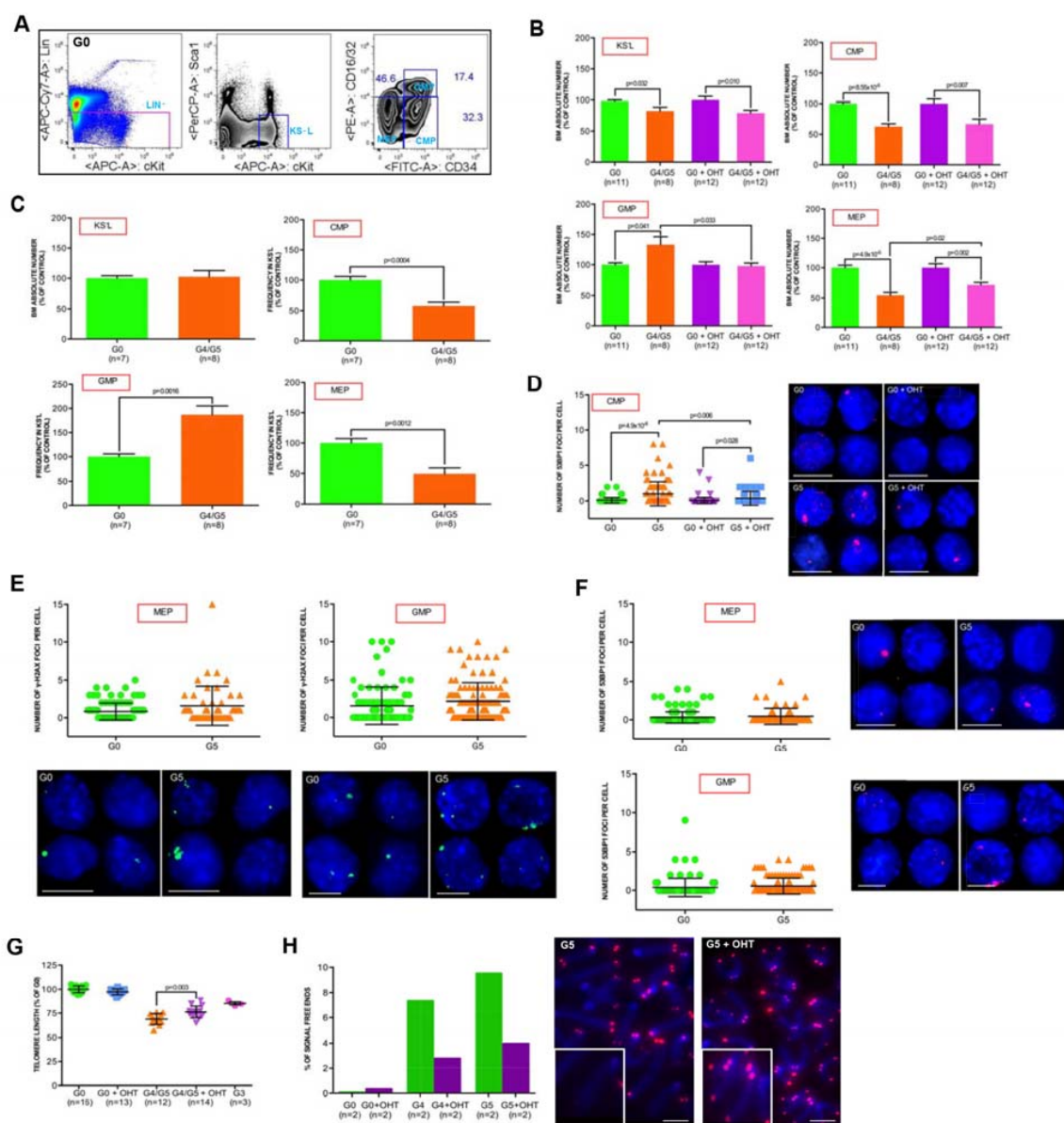
Figure S1, related Figure 1. The hematopoietic compartment of telomere dysfunctional mice recapitulates hallmark features of human myelodysplastic syndrome.

(A) Active caspase 3 immuno-stained section of a representative G5 BM biopsy (left panel) or irradiated (IR) wild type BM biopsy used as positive control (right panel) (scale bar, 15 μ m).

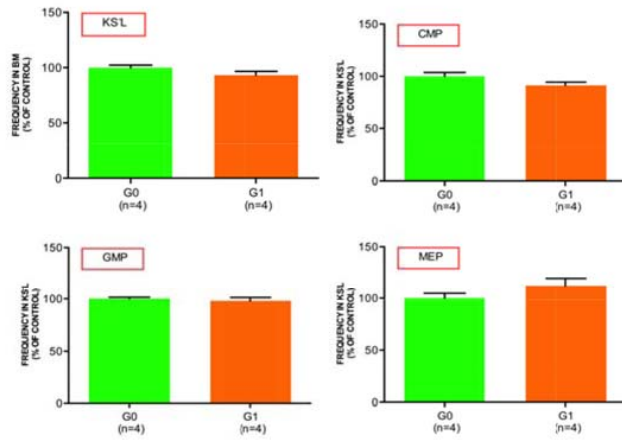
(B) Representative G5 BM cytopsin stained with Prussian blue. Iron deposits do not surround the perinuclear membrane indicating the absence of ring sideroblasts (scale bar, 15 μ m).

(C) Cytogenetic analysis of G4/G5 TERT^{ER/ER} BM cells showed chromosomal breaks and fusions (on the left); representative G5 metaphase spread (on the right).

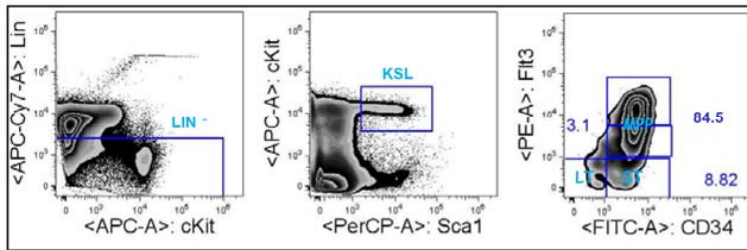
(D) Karyotype of a representative G5 mouse with a clonal robertsonian translocation t(8;12).



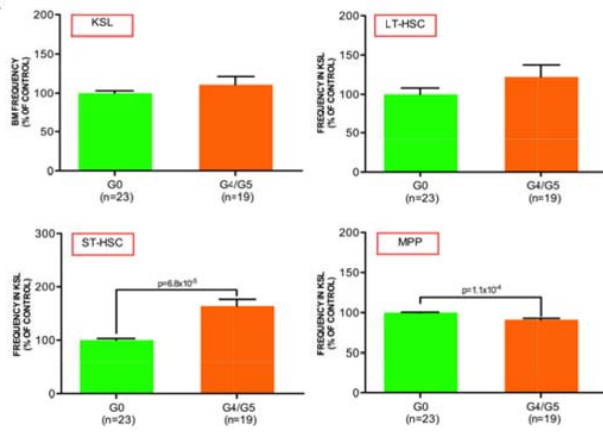
I



J



K



L

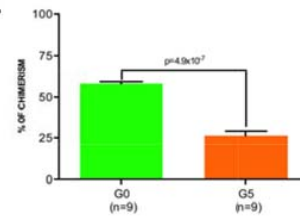


Figure S2, related to Figure 2. Skewed myeloid-erythroid differentiation of CMP is reversed by telomerase reactivation.

(A) Lineage negative (Lin⁻), KS⁻L, CMP, GMP and MEP representative profiles.

(B) KS⁻L, CMP, GMP and MEP absolute numbers in the BM of indicated genotypes and treatments (mean and s.e.m. of age-matched 3 month-old mice from 3 independent experiments of telomerase reactivation *in vivo*; data are expressed as percentage of corresponding controls).

(C) KS⁻L absolute number, as well as CMP, GMP and MEP frequencies in the KS⁻L population of age-matched 7 month-old mice of indicated genotypes (data are expressed as percentage of the G0 control; error bars denote s.e.m).

(D) Anti-53BP1 immunofluorescence in CMP sorted from mice of indicated genotypes and treatments (α -53BP1: red; DAPI: blue; scale bar, 20 μ m; n=4; right panel); numbers of 53BP1 foci per cell (left panel) (error bars denote s.d).

(E) Anti- γ H2AX immunofluorescence in MEP (on the left) and GMP (on the right) sorted from mice of indicated genotypes (α - γ H2AX: green; DAPI: blue; scale bar, 10 μ m; n=4, bottom panel); numbers of γ H2AX foci per cell (upper panel) (error bars denote s.d.).

(F) Anti-53BP1 immunofluorescence in MEP and GMP sorted from mice of indicated genotypes (α -53BP1: red; DAPI: blue; scale bar, 10 μ m; n=4, right panel); numbers of 53BP1 foci per cell (left panel) (error bars denote s.d.).

(G) Mean value of telomere length in primary BM cells of indicated genotypes and treatments, as determined by flow-FISH analysis (mean and s.e.m of mice from 3 independent experiments of telomerase reactivation *in vivo*; data are expressed as percentage of the G0 control).

(H) Representative signal free ends in primary BM metaphases of indicated genotypes, 20 metaphases/sample; BM cells from two G0, one G4 and one G5 mice were analyzed after vehicle or OHT treatment (left panel); representative G5/vehicle or G5/OHT-treated BM metaphases (right panel) (scale bar, 1 μ m).

(I) KSL frequency in the BM, as well as the CMP, GMP and MEP frequencies in the KSL population of G0 or G1 mice (mean and s.e.m. of age-matched 3 month-old mice; data are expressed as percentage of corresponding controls).

(J) Lineage negative (Lin⁻), KSL, LT-HSC, ST-HSC and MPP representative profiles.

(K) KSL frequency in the BM, as well as the LT-HSC, ST-HSC and MPP frequencies in the KSL population of indicated genotypes (mean and s.e.m. of age-matched 3 month-old mice from 6 independent experiments; data are expressed as percentage of corresponding controls).

(L) Repopulation capacity of G0 or G5 LT-HSC was determined in experiments of competitive transplantation using CD45.1- and CD45.2-specific antibodies (mean and s.e.m. of n=9 recipient mice/ group). Shown is the percentage contribution of donor cells two months after transplantation. Similar results were obtained 4 months after transplantation (data not shown).

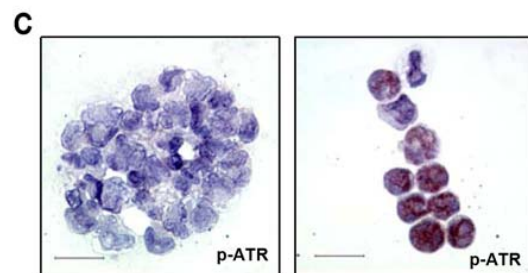
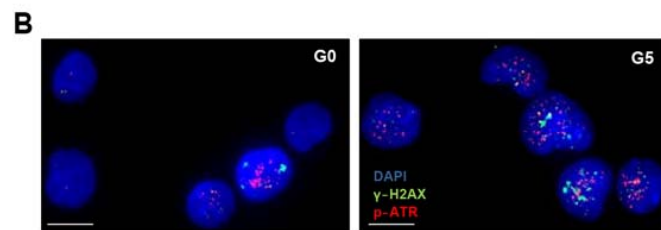
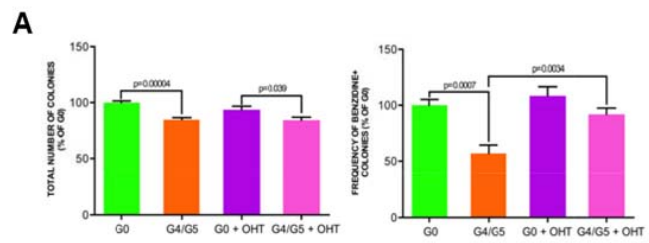


Figure S3, related to Figure 3. Defective CMP differentiation is due to cell intrinsic DNA damage signaling activation.

(A) Clonogenic myeloid colony formation in methylcellulose from MNCs of indicated genotypes cultured in the presence of vehicle or OHT: total number of colonies (left panel) and frequency of benzidine positive colonies (right panel) (mean and s.e.m of replicates from 2 independent experiments; each experiment includes MNCs obtained from a pool of 3 mice of indicated genotypes; data are expressed as percentage of G0 control).

(B) Representative anti-p-ATR immunofluorescence in CMP sorted from G0 (on the left) or G5 (on the right) mice; α - γ H2AX: green; α -p-ATR: red; DAPI: blue; (scale bar, 20 μ m).

(C) Representative anti- p-ATR immunohistochemistry of CD34⁺ cells isolated from a lower (on the left) or a higher risk MDS patient (on the right) (scale bar, 15 μ m).

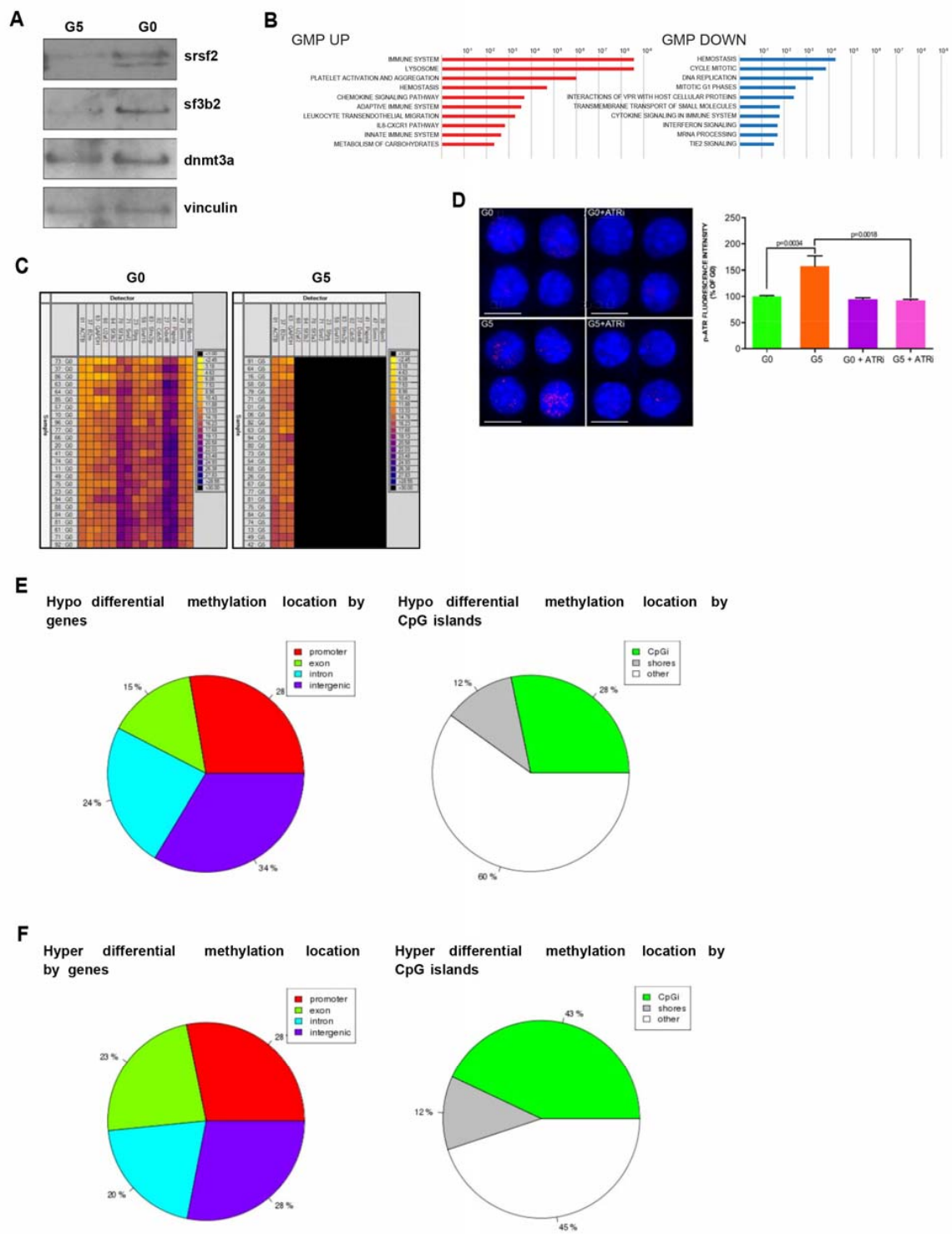


Figure S4, related to Figure 4. Telomere dysfunction induces aberrant RNA splicing by repressing splicing gene expression in CMP.

(A) Representative western blot analysis of *srsf2*, *sf3b2*, *dnmt3a* and vinculin proteins in 25,000 CMP isolated from a pool of 4 G0 or G5 mice. To show the concomitant downregulation of multiple splicing factors and *dnmt3a*, protein detection was performed on the same G0 and G5 CMP sample.

(B) Significantly downregulated and upregulated pathways identified by GSEA in G4/G5 compared to G0 GMP (FDR =0.05).

(C) Fluidigm-based gene expression analysis of single cells (rows) for representative genes in the mRNA processing / spliceosome pathways (columns), which are significantly altered in sorted CMP from the G0 and G5 mice after LT-HSC transplantation in wild type mice (n=3). Genes analyzed were (from left to right): *ACTB*, $\beta 2m$, *GAPDH* (housekeeping genes; internal controls), *U2AF2*, *SF3B2*, *SF3A3*, *SRSF2*, *SFPQ*, *SFRS10*, *SFRS2IP*, *CDC51*, *DDX46*, *PAPOLA*, *SRRM1* and *RBM5*. Donor cells were identified by staining with anti-CD45.2 antibody. Color scale on the right shows correspondence between color code and Ct values.

(D) Representative anti-p-ATR immunofluorescence in CMP sorted from G0 or G5 mice with or without ATR inhibitor treatment (α -p-ATR: red; DAPI: blue; left panel; scale bar, 20 μ m); p-ATR fluorescence intensity in CMP sorted from G0 or G5 mice with or without ATR inhibitor treatment (mean and s.e.m of cells from a pool of 2 or 3 mice for each condition; data are expressed as percentage of G0 control; panel on the right).

(E) On the left: pie charts illustrating the proportion of differentially hypo-methylated CpGs on promoter regions (red), exons (green), introns (blue) and intragenic regions (magenta); on the

right: pie charts illustrating the proportion of differentially hypo-methylated CpGs on CpG islands (green), CpG island shore (grey), and other regions (white).

(F) On the left: pie charts illustrating the proportion of differentially hyper-methylated CpGs on promoter regions (red), exons (green), introns (blue) and intragenic regions (magenta); on the right: pie charts illustrating the proportion of differentially hyper-methylated CpGs on CpG islands (green), CpG island shore (grey), and other regions (white).

Table S1, related to Figure 4. List of probes down-regulated and up-regulated in G4/G5 CMP.

Table S2, related to Figure 4. List of genes validated by single cell Fluidigm Real Time-PCR.

Table S3, related to Figure 4. List of aberrantly spliced exons in G4/G5 as compared to G0 CMP ($p < 0.05$).

Table S4, related to Figure 4. Predicted consequences of aberrant splicing on transcripts leading to frameshifts or loss of ATG / STOP codons, thereby impairing protein function.

Table S5, related to Figure 4. List of transcripts (with intact ATG and STOP codons) that are predicted to lose known protein domains due to aberrant splicing.

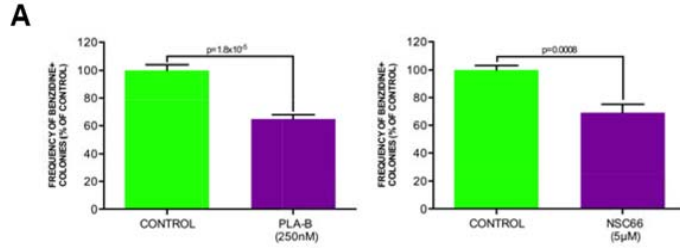


Figure S5, related to Figure 5. *SRSF2* haploinsufficiency induces skewed myeloid differentiation of CMP.

(A) Clonogenic myeloid colony formation in methylcellulose from sorted G0 CMP pre-treated with vehicle, Pladienolide B (PLA-B, 250 nM, left panel) or NSC663284 (NSC66, 5 µM, right panel) for 4 hr. Erythroid cells were scored by benzidine staining and expressed as frequency of the total number of colonies (mean and s.e.m of replicates from 2 independent experiments; each experiment includes CMP sorted from a pool of 3 wild type mice; data are expressed as percentage of vehicle control).

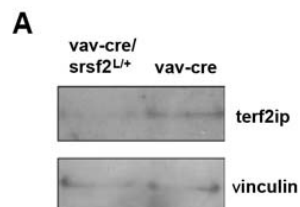


Figure S6, related to Figure 6. Aberrant RNA splicing due to reduced *SRSF2* expression induces telomere dysfunction.

(A) Representative western blot analysis of TERF2IP and vinculin proteins in 25,000 CMP isolated from a pool of 4 *Vav-cre* or *Vav-cre/ SRSF2^{L/+}* mice.

Table S6, related to Figure 6. List of aberrantly spliced exons in *Vav-cre/ SRSF2^{L/+}* as compared to *Vav-cre* CMP (p <0.05).

Table S7, related to Figure 6. List of aberrantly spliced exons in CD34⁺ CMML cells with *SRSF2*(P95) mutation as compared to CD34⁺ CMML cells without mutation (p<0.01).

SUPPLEMENTAL EXPERIMENTAL PROCEDURES

Generation and analysis of mice

Mice were maintained in specific pathogen-free (SPF) conditions at MD Anderson Cancer Center. All manipulations were performed with IACUC approval. The heterozygous (G0 TERT^{ER/+}) and late generation homozygous (G4/G5 TERT^{ER/ER}) mice were generated based on standard breeding protocol of successive generations of telomerase-deficient mice (Sahin et al., 2011). All studies were performed on adult (12-16 week old) G0 TERT^{ER/+} and telomere dysfunctional G4/G5 TERT^{ER/ER} mice, unless otherwise noted. OHT time-release pellets (2.5 mg; Innovative Research of America) were inserted subcutaneously to reach steady state blood levels of 1 ng ml⁻¹ OHT.

Due to the variability in telomere length in the G4/G5 TERT^{ER/ER} cohort, about 20 mice per group were used in the telomerase reactivation experiment for hematological characterization. Age- and gender-matched mice were randomly chosen for either placebo or OHT treatment. The *in vivo* experiments were not performed blinded. For mechanistic studies, G4/G5 TERT^{ER/ER} mice with obvious defective hematopoiesis from CBC analysis were used.

The ATR inhibitor VE-821 (Selleck Chemicals) was dissolved in 0.5% methylcellulose and administered to the G0 or G5 mice by oral gavage at a concentration of 60 mg/kg. The drug was administered to the mice at a volume of 10 µl per 1 g body weight. Mice were sacrificed and analyzed 24 hours later.

The conditional deletion of *SRSF2* in the hematopoietic compartment was accomplished by crossing *Vav-cre* mice (Jackson laboratories) with the *SRSF2*^{L/L} mice (Jackson laboratories) to generate heterozygous *Vav-cre/ SRSF2*^{L/+} mice.

Peripheral blood samples were collected in EDTA-coated tubes and complete blood count (CBC) was performed with an automated Hemavet hematology analyzer through the Department of Veterinary Medicine and Surgery Histopathology Core at MDACC. Animals were autopsied, and the BM and spleen tissues were examined regardless of their pathological status. Tissue samples were fixed in 10% neutral-buffered formalin (Sigma) overnight, and washed once with 1× PBS and then transferred into 70% ethanol and stored at 4°C. Tissues were processed by ethanol dehydration and embedded in paraffin according to standard protocols. Sections (3 µm) were prepared for antibody detection and haematoxylin and eosin staining.

Morphological evaluation and cytochemical stains

Cytospins of BM cells were prepared following standard procedure, fixed in methanol for 7 min and stained using the Giemsa-Wright method or Prussian blue. Cytochemical assays involved tests for myeloperoxidase (Sigma) and nonspecific esterase (α -naphthyl butyrate, Sigma) activity.

Histological analysis

Paraffin embedded BM and splenic sections were used for chromogenic immunohistochemistry, which was performed according to standard procedures. Antibodies used include myeloperoxidase (MPO, catalog number RB373R7, Thermo Scientific Lab Vision), CD11b (clone number EPR1344, Abcam), Cleaved Caspase-3 (catalog number CP229, Biocare Medical) and Ter119 (clone number TER-119, BD Pharmingen).

Cytogenetic analysis

Bone marrow single-cell suspensions isolated from 1 tibia were cultured overnight and treated with KaryoMAX Colcemid solution (Invitrogen) for 2 h before collection. Telomere fluorescence *in situ* hybridization (FISH) was performed on metaphase nuclei, as described previously (Maser et al., 2007). At least 20 metaphases from harvested cell cultures were analyzed for telomere integrity by telomere-specific peptide nucleic acid (PNA)-FISH. Telomere signal was normalized using a Pacific Blue centromeric PNA probe. Telomere length of the BM cells was also confirmed by using the DAKO Telomere PNA Kit/FITC for Flow Cytometry (DAKO). Relative telomere length (RTL) was determined by comparing isolated test cells with a control cell line (1301; subline of the Epstein–Barr virus (EBV) genome negative T-cell leukemia line CCRF-CEM, Sigma). Cells were STR profiled and tested mycoplasma negative.

Flow cytometry analysis

Single-cell suspensions were prepared from spleen and bone marrow (from femoral and tibial bones) by passing cells through pre-separation filters (Miltenyi). Cell numbers were subsequently counted. For FACS sorting and analysis we used described staining protocols and published stem and progenitor cell definitions (Amrani et al., 2011; Flach et al., 2014). Cells were acquired using LSR Fortessa (BD Bioscience) or sorted by Influx Cell Sorter (BD Bioscience) and analyzed using FlowJo software (Tree Star). Cell doublets were excluded from all analyses and dead cells were excluded by the use of DAPI. For splenic preparations, RBCs were lysed before antibody staining. Lin⁻ cells were enriched using a lineage cell depletion kit (Miltenyi) and an anti-CD127 (clone number A7R34) antibody conjugated to biotin. The following antibodies (all from eBioscience, BD Pharmingen or Biolegend) conjugated to FITC, APC, PE, PercpCy5.5, BV421, BV605 or APC-Cy7 were used for the flow cytometry analysis: -

TER119 (clone number TER-119), -CD71 (clone number R17217) -CD16/CD32 (clone number 93), -c-Kit (clone number 2B8), -Sca-1 (clone number D7), -CD34 (clone number RAM34), -Streptavidin, -Flk2 (clone number A2F10).

Absolute numbers were calculated based on BM cellularity of 4 hinds limbs, frequency of specific progenitor populations, and weight of individual animals to normalize for differences in body size, and presented as % of corresponding controls, as previously reported (Rossi et al., 2007).

In experiment of transplantation, donor and recipient cells were identified by staining with anti-CD45.2 (clone number 104) or CD45.1 (clone number A20) antibodies, respectively.

Indirect immunofluorescence microscopy and Tif assay

Sorted progenitor cells were resuspended in PBS, spotted on immunofluorescence slides (ThermoScientific), fixed for 30 min in 4% paraformaldehyde (Sigma-Aldrich), permeabilized in 0.2% Triton X-100 for 5 min and blocked in 5% Bovine Serum Albumin for 1 hour. Then, cells were stained with anti γ H2AX (1:200; clone number JBW301, Millipore), 53BP1 (1:200, catalog number IHC00001, Bethyl Laboratories) or phospho-ATR (1:50; catalog number 2853, Cell Signaling) primary antibodies. Alexa Fluor-555 and Alexa Fluor-488 (Life Technologies) were used as secondary antibodies. Nuclei were stained with DAPI (Sigma-Aldrich). For every staining, the analysis was performed blinded with 4 mice of different genotypes or treatments.

For Tif assay, cells were co-stained with γ H2AX and the telomere specific PNA probe using the Telomere PNA FISH Kit/Cy3 (DAKO, Glostrup, Denmark), according to the manufacturer's instructions. Coverslips were mounted with Prolong Gold Antifade reagent (Life Technologies).

Images were collected in Widefield Microscopy (Nikon Instruments Inc.) and analyzed using ImageJ software (<http://rsbweb.nih.gov/ij/>).

Treatments and colony forming assay

Mononuclear cells (MNCs) (20×10^4 /replicate) or sorted CMP (500 cells/replicate) were seeded into cytokine supplemented methylcellulose medium (Methocult, M3434, Stem Cell Technologies). In separate experiments sorted CMP were pre-treated with a specific inhibitor of ATR (EMD Millipore 118510, 1 μ M) or ATM (EMD Millipore 118500, 2 μ M) for 1 hour, cisplatin (Sigma, 5 μ M), pladienolide B (Bioaustralis Fine Chemicals, 250nM) or NSC663284 (Sigma, 5 μ M) for 4 hours, washed and seeded in methylcellulose. In experiments of irradiation wild type mice were irradiated with γ radiation (3Gy) and CMP were sorted after 15 hours or 4 months in long-term experiments. In experiments of telomerase reactivation, MNCs or CMP were cultured in the presence of vehicle or OHT (Sigma, 100 nM). Colonies were counted after 7-10 days. Erythroid cells were scored by benzidine staining.

LTC-IC assay

Stromal layers were prepared from bone marrows isolated from wild type mice, cultured in 12.5% horse-serum IMDM supplemented with 12.5% FBS, penicillin, streptomycin, 1 μ M hydrocortisone and 50 μ M 2-mercaptoethanol at 37°C. After 3 weeks, confluent stromal layers were trypsinized, irradiated (15 Gy) and subcultured in 6 multiwell plates. Cultures were then seeded with bone marrow MNCs (2.5×10^5 per well) in the presence of vehicle or OHT (100 nM). Cells derived from 5-week LTC-IC were seeded in cytokine supplemented

methycellulose medium (Methocult, M3434, Stem Cell Technologies). Colonies were scored after 10–14 days.

Immunocytochemical analysis

Immunocytochemical analysis was performed in cytospin preparations of CD34⁺ cells according to standard procedures. Cells were stained with anti-pATR antibody (1:50, catalog number 2853, Cell Signaling). Correlation between ATR phosphorylation and IPSS risk was evaluated using Fisher's exact test.

Quantitative real-time PCR (qPCR) in human MDS CD34⁺ cells

After purification, CD34⁺ cells were lysed with Trizol, according to the manufacturer's specifications for RNA extraction. Purified RNA was dissolved in sterile distilled water. cDNA was synthesized using High Capacity cDNA Reverse Transcription Kit (Applied Biosystems, Carlsbad, CA), according to the manufacturer's protocol and using 200 ng of RNA per reaction. Q-PCR reactions were performed using TaqMan Expression Assays for *Srsf2* and *gapdh* genes (Applied Biosystems) and TaqMan Universal PCR Mastermix (Applied Biosystems) in a 7500 Real-Time PCR System (Applied Biosystems). Each condition was run in duplicate. Expression levels of *Srsf2* were normalized to those of *Gapdh*.

Single-cell gene expression profiling

Single CMP cells were sorted directly into 96-well plates in the Cells Direct Reaction Mix (Invitrogen). Individual cell lysis, cDNA synthesis, and amplification were performed according to Fluidigm Advanced Development Protocol, and single-cell microfluidic real-time PCR using

Dynamic Array IFCs (Biomark Fluidigm) was performed. Pre-amplified products (22 cycles) were diluted fivefold before analysis with Universal PCR Master Mix and pre-designed primers (DELTAgene Assays, Fluidigm) in 96.96 Dynamic Arrays on a BioMark System (Fluidigm). Primer sequences used in this study are available upon request. Ct values were calculated from the system's software (BioMark Real-time PCR Analysis; Fluidigm) and filtered according to a set of quality control rules. Gene filter: (1) for each gene, including controls, data with CtCall = FAILED and CtQuality \leq threshold were removed. (2) For each gene, including controls, genes with a difference of duplicate CtValues \geq 2.0 were considered inconsistent and removed. Sample filter: (1) if the control genes (*Gapdh*, *B2m* and *Actb*) were not expressed or removed according to gene filters, the whole sample was removed. (2) If the mean of the Ct values of all genes including controls in a row was \geq 27.0 the whole sample row was removed. To estimate for relative fold changes between control vs. G5 CMP, an arbitrary value of 30 is assigned if the intensity of the probe is read as "999" from the instrument.

Microarray and pathway analysis

Bone marrow CMP and GMP cells were sorted from 2 paired pools of G0 TERT^{ER/+} or G4/G5 TERT^{ER/ER} mice (5,000-20,000 cells per sample) using the Influx Cell Sorter. Every paired pool includes CMP and GMP sorted from 4 age and gender matched G0 or G4/G5 mice. RNA from the respective sorted cells was extracted using Trizol (Ambion) and profiled on 2100 Bioanalyzer (Agilent). Gene expression profiling was performed at the Sequencing and Non-coding RNA Program at MD Anderson Cancer Center. Briefly, the GeneChip® 3' IVT Express Kit (Affymetrix) was used to generate biotin-labeled cRNA, which were purified and fragmented, before target hybridization on the GeneChip® Mouse Genome 430 2.0 Array

(Affymetrix) according to the manufacturer's instructions. Affymetrix raw data (CEL files) were normalized using Affymetrix Microarray Suite (MAS) version 5.0. Due to the low number of replicates, differentially expressed genes were identified using an arbitrary fold change of 1.3 in paired pools. To identify pathways that were enriched in the sorted G4/G5 TERT^{ER/ER} CMP and GMP cells, Gene Set Enrichment Analysis (GSEA; <http://www.broadinstitute.org/gsea/msigdb/annotate.jsp>) was performed on genes which were consistently upregulated or downregulated in both G4/G5 CMP samples when compared to the respective G0 controls in a pairwise manner.

RNA-Seq sequencing and analysis

Total RNA from sorted CMP isolated from 3 independent G0 TERT^{ER/+} and 4 G4/G5 TERT^{ER/ER}, 3 *Vav-cre* and 6 *Vav-cre/ SRSF2^{L/+}* mice, as well as CMML patient-derived CD34⁺ cells (n=15) was isolated by Trizol (Ambion) and profiled on 2100 Bioanalyzer (Agilent). About 1 ng total RNA was amplified using the Ovation® RNA-Seq System V2 kit (Nugen), and libraries constructed using Ovation® Ultralow Library Systems and Ovation® Ultralow DR Multiplex System 1–8 (Nugen) according to the manufacturer's instructions. Transcriptomic sequencing (RNA-Seq) was performed on the Illumina HiSeq platform using the standard paired-end protocol. In total 60-160 million 76 base pair (bp) reads were generated per sample. An initial sequence-level quality assessment was performed using FastQC (version 0.10.1, Simon Andrews). The RNA-seq reads were then mapped to the mouse (NCBI Build 37.2) or human (GRCh37) reference genome using Tophat2, allowing a maximum of two mismatches per 75 bp sequencing end. The NCBI RefSeq gene model and HTSeq software (version 0.5.4p2, Simon Anders) were used to quantify the gene-level expression, exon-specific expression and intron

retention levels. The differential analyses for gene/isoform expression and intron retention were analyzed with DESeq2 (Anders and Huber, 2010), while exon usage was analyzed with DEXSeq (Anders et al., 2012). For an aberrantly spliced exon to be considered statistically significant relative to the controls, the criteria of $P < 0.05$ (in the G0 versus G4/G5 or *Vav-cre* versus *Vav-cre/Srsf2*^{L/+} CMP analyses) or $P < 0.01$ (in the mutant *Srsf2* versus not mutant *Srsf2* CD34⁺ cell analysis) was employed. Pathway enrichment analysis was performed with Pathway Studio (version 10.2.2.9, Elsevier Inc.). Perl scripts were written to predict the effects of loss of exon on the protein sequences encoded. Domain prediction was performed using Pfam, and E-val ≤ 0.01 was considered significant.

Reduced representation bisulfite sequencing (RRBS)

Genomic DNA was extracted from sorted CMP populations isolated from 3 pools of G0 or 2 pools of G4/G5 mice using UltraPure™ Phenol:Chloroform:Isoamyl Alcohol according to manufacturer's instructions (Life Technologies). 14,000 to 30,000 cells were available for each sample, resulting in a minimum of 45ng of DNA. Genome-wide DNA methylation profiling was performed by RRBS. Library preparation and sequencing were performed at the UT MD Anderson Cancer Center's DNA Methylation Analysis Core and Sequencing and Microarray Facility, according to published protocols (Gu et al., 2011). RRBS sequencing data were aligned and methylation was called using Bismark v0.7.11 (Krueger and Andrews, 2011). In brief, bisulphite-treated DNA was aligned to UCSC Genome Browser mm10 reference genome using Bowtie. In total 29-38 million reads were generated per sample with alignment rates around 63%. Next, MethylKit (Akalin et al., 2012) implemented with Fisher's exact test was used to compare the cytosine methylation profiles of G0 and G5 CMP. Gene promoter regions were

calculated based on RefSeq gene annotations with regions starting 1 kb upstream of the annotated transcription start site (TSS) and extending 500 base pairs downstream of TSS. Exons, introns, and CpG islands coordinates were collected from the UCSC Genome Browser mm10 version.

Western blotting

Western blotting in small amount of cells was performed as previously described (Nakada et al., 2010). Briefly, the same number of CMP (25,000 cells) purified from a pool of 4 G0 and G4/G5 or *Vav-cre* and *Vav-cre/ SRSF2^{L/+}* mice was sorted into Trichloroacetic acid (TCA) and adjusted to a final concentration of 10% TCA. Extracts were incubated on ice for 30 minutes and spun down for 10 minutes at 16.1 rcf at 4°C. The supernatant was removed and the pellets were washed with acetone twice then dried. The protein pellets were solubilized with Solubilization buffer (9 M Urea, 2% Triton X-100, 1% DTT) before adding LDS loading buffer. Proteins were separated on a Bis-Tris polyacrylamide gel (Invitrogen) and transferred to a PVDF membrane. Antibodies were anti-sfrs2 (clone number 1SC-4F11, Millipore), anti-sf3b2 (clone number 5D2, Sigma), anti-dnmt3a (clone number H-295, Santa Cruz), anti terf2ip (clone number D9H4, Cell Signaling) and anti-vinculin (clone number hVIN-1, Sigma).

Bone Marrow Transplantations

Experiments of BM transplantation were performed as previously described (Sahin et al., 2011). Briefly, CD45.1⁺ recipient mice (Jackson Laboratories) were irradiated with a total of 10.5 Gy γ -radiation (5 Gy and 5.5 Gy 3 hours apart) on the day of transplantation. BM transplants were performed using purified LT-HSC (1,500 cells / mouse) isolated from a pool of 3 G0 or

G5 TERT^{ER/ER} (all CD45.2+) donor mice. Competitive blood repopulation was performed by mixing the specified CD45.2 cells together with nucleated bone marrow cells prepared from congenic CD45.1 mice. Specifically, each recipient received 1,500 purified LT-HSC derived from a pool of 3 G0 or G5 TERT^{ER/ER} mice together with 3×10^5 CD45.1 competitor bone marrow cells. Donor derived peripheral blood reconstitution (i.e. chimaerism) was assessed after 2 or 4 months following transplantation by FACS analysis of nucleated peripheral blood cells stained with anti-CD45.1 and anti-CD45.2-specific antibodies. Blood chimaerism for each recipient was calculated as the percentage of all CD45+ cells that were CD45.2+.

Statistical analysis

All the cytogenetics, indirect immunofluorescence microscopy, immunohistochemistry, and Fluidigm PCR analyses were performed blinded without the investigator knowing the sample annotation and outcome.

All the data were analyzed by a two-tailed Student's *t*-test ($p < 0.05$ is considered to be statistically significant). For all experiments with error bars, standard error mean was calculated to indicate the variation within each experiment and data, and values represent mean \pm s.e.m or mean \pm s.d., as indicated in the figure legends. Variance within each group of data was not evaluated and final data was analyzed by pooling biological replicates from different experiments.

SUPPLEMENTAL REFERENCES

Akalin, A., Kormaksson, M., Li, S., Garrett-Bakelman, F.E., Figueroa, M.E., Melnick, A., and Mason, C.E. (2012). methylKit: a comprehensive R package for the analysis of genome-wide DNA methylation profiles. *Genome biology* 13, R87.

Gu, H., Smith, Z.D., Bock, C., P., B., Gnirke, A., and Meissner, A. (2011). Preparation of reduced representation bisulfite sequencing libraries for genome-scale DNA methylation profiling. *Nature Protocol* 6, 468-481.

Krueger, F., and Andrews, S.R. (2011). Bismark: a flexible aligner and methylation caller for Bisulfite-Seq applications. *Bioinformatics* 27, 1571-1572.

Maser, R.S., Wong, K.K., Sahin, E., Xia, H.L., Naylor, M., Hedberg, H.M., Artandi, S.E., and DePinho, R.A. (2007). DNA-dependent protein kinase catalytic subunit is not required for dysfunctional telomere fusion and checkpoint response in the telomerase-deficient mouse. *Molecular and Cellular Biology* 27, 2253-2265.